Modification of Saharan air layer and environmental shear over the eastern Atlantic Ocean by dust-radiation effects

Shu-Hua Chen,[1] Sheng-Hsiang Wang,[2,3] and Mark Waylonis[1]

Received 8 March 2010; revised 9 July 2010; accepted 21 July 2010; published 4 November 2010.

[1] This study investigates the influence of dust-radiation effects on the modification of the Saharan air layer (SAL) and environmental shear. A tracer model based on the Weather Research and Forecast model was developed to examine the influence using a dust outbreak event. Two numerical experiments were conducted with (ON) and without (OFF) the dust-radiation effects. Both simulations reasonably reproduced SAL's features. However, the 700 hPa maximum temperature within SAL was slightly underestimated and shifted northwestward from OFF. These were improved from ON, but the maximum temperature became slightly overestimated, which might be due to inaccurate optical properties. The dust-radiation interactions mainly warmed the dusty air between 750 and 550 hPa because dust shortwave absorption dominated dust longwave cooling. Another major warming area was found near the surface over the ocean due to longwave radiative heating by dust aloft. The modification of temperature resulted in an adjustment of the vertical wind shear. To the south of SAL, where easterly wave disturbances and tropical storms usually occur, the vertical zonal wind shear increased by about 1~2.5 m s^{-1} km^{-1} from 750 to 550 hPa, resulting in a maximum wind change of 3~5 m s^{-1}, a 30~40% increase, around the top of this layer. The enhancement of the vertical shear in this layer could potentially have an impact on TC genesis and development. The dust-radiation effects also modified the moisture and dust distribution, which can have a feedback (i.e., a secondary effect) on the heating profile and the vertical shear.

Citation: Chen, S.-H., S.-H. Wang, and M. Waylonis (2010), Modification of Saharan air layer and environmental shear over the eastern Atlantic Ocean by dust-radiation effects, *J. Geophys. Res.*, *115*, D21202, doi:10.1029/2010JD014158.

1. Introduction

[2] Tropical cyclones (TCs) at landfall are one of the most dangerous natural disasters. Accurate TC data analysis and forecasts are crucial for the protection of life and property. In the past two decades, advances in remote sensing observations (e.g., satellites), theoretical studies, numerical modeling, and data assimilation techniques have improved our understanding of TC dynamics and thermodynamics. Interestingly, although TC track forecasts in the past decade have been significantly improved, intensity forecasts still remain unsatisfactory [e.g., *Krishnamurti et al.*, 2005; *Rogers et al.*, 2006; *Mainelli et al.*, 2008], particularly during the rapid intensification period. This has been partially attributed to insufficient resolution of the numerical models, imperfect parameterization of physical processes, incomplete understanding of the multiscale interactions within hurricanes, etc. [*Krishnamurti et al.*, 2005; *Mainelli et al.*, 2008].

[3] Research activities and field experiments have also expanded to the earlier stages of TC life cycles, such as TC genesis [*Zipser et al.*, 2009]. TC genesis is strongly influenced by environmental factors, such as the sea surface temperature (SST), moisture in the lower troposphere, and vertical wind shear [*Gray*, 1968]. *Landsea* [1993] revealed that the majority of intense hurricanes over the Atlantic Ocean originated from African easterly waves. Satellite data, field experiments, and numerical studies have shown the potential influence of the Saharan air layer (SAL) on TC activities, both positive and negative [*Karyampudi and Carlson*, 1988; *Karyampudi and Pierce*, 2002; *Dunion and Velden*, 2004; *Evan et al.*, 2006; *Jones et al.*, 2007; *Wu*, 2007; *Shu and Wu*, 2009; *Sun et al.*, 2008, 2009; *Pratt and Evans*, 2009; *Reale et al.*, 2009]. However, controversial studies for such an influence have also been presented [*Braun*, 2010], and more studies on this are required.

[4] Saharan dust, often propagating downstream along SAL to the Atlantic Ocean, can modify the SAL and its environment by changing the energy budget through direct and indirect radiative forcing. Scattering by suspended dust directly impacts atmospheric radiation fluxes, modifying the energy budget in the atmosphere and on the surface. These dust-radiation effects potentially increase the amplitude of easterly waves [*Jones et al.*, 2004]. Smaller dust particles remain

[1]Department of Land, Air, and Water Resources, University of California, Davis, California, USA.
[2]Department of Atmospheric Sciences, National Central University, Chung-Li, Taiwan.
[3]Goddard Space Flight Center, NASA, Greenbelt, Maryland, USA.

0148-0227/10/2010JD014158

suspended in the air for a longer time period. These fine particles can potentially reach an altitude of 8–9 km [*Liu et al.*, 2003], where they nucleate ice crystals and transform cloud microphysical properties, indirectly changing the energy budget. The modification of the energy budget within and around the SAL, one of the TC's immediate environments, can potentially affect TC evolution through dust-cloud-radiation interactions. For example, using satellite data, *Evan et al.* [2006] showed that the number of TC days inversely correlates to dust coverage over the eastern to middle Atlantic Ocean.

[5] Several studies have examined the dust-radiation effects [*Carlson and Benjamin*, 1980; *Wong and Dessler*, 2005; *Zhu et al.*, 2007; *Wong et al.*, 2009]. Under cloudless conditions with an elevated dust plume (e.g., a Saharan dust plume over the eastern Atlantic Ocean), dust absorption of shortwave radiation creates a heating effect around the dust maxima, while dust extinction reduces the radiative flux, creating a cooling effect below. For longwave radiation, dust absorbs and reflects energy from below and then re-emits longwave in all directions, similar to a greenhouse gas; this results in a cooling effect in the dusty layer, with the maximum cooling slightly above the maximum dust concentration, and a warming effect near the surface. For the combination of dust-longwave and shortwave interactions, around the maximum dust concentration the net effect is dominated by the dust-shortwave radiation interaction, resulting in net heating with the maximum occurring slightly below the peak dust concentration, while below the net effect is dominated by longwave radiation processes, also resulting in net heating near the surface [*Carlson and Benjamin*, 1980; *Zhu et al.*, 2007; *Wong et al.*, 2009]. The dryness of the SAL can also play a role in modifying the temperature profile, as the absorption of longwave radiation is reduced [*Wong et al.*, 2009]. Therefore, high aerosol optical thickness below 700 hPa is associated with increased atmospheric stability through increased temperature and dryness, suppressing convection as a result [*Wong and Dessler*, 2005; *Wong et al.*, 2009].

[6] The magnitude of the radiative impact of dust is highly dependent upon the dust optical characteristics used in the calculation, such as particle size distribution [*Tegen and Lacis*, 1996] and dust refractive indices. Recent studies have updated information about the complex part of the refractive index of Saharan dust. *Colarco et al.* [2002] used modeled Saharan dust to simulate backscatter radiances, which were used to construct a Total Ozone Mapping Spectrometer (TOMS) aerosol index. In their study, they inferred that the imaginary part of refractive indices used by TOMS at 331 and 360 nm was too large, and would make modeled absorption by dust too strong. *Sinyuk et al.* [2003] used observational radiances at 331 and 360 nm from TOMS in combination with aerosol optical depth (AOD) measurements from the Aerosol Robotic Network (AERONET) to study the imaginary refractive index of Saharan dust at these wavelengths. They similarly found that previous studies overestimated the imaginary refractive index at these wavelengths. As a result, the optical coefficients used in the present study may cause the shortwave absorption by dust to be overestimated; yet, this study's qualitative conclusions about dust-radiation interactions should be unaffected. *Wong et al.* [2009] used more updated optical properties, yet their qualitative results were consistent with *Carlson and Benjamin* [1980], whose shortwave heating was overestimated. More recent studies have been conducted on the properties of Saharan dust. For instance, *Chen et al.* [2010] extensively studied particle size and number distributions, scattering properties at several different wavelengths, and microphysical properties using in situ measurements as part of the NASA African Monsoon Multidisciplinary Analysis.

[7] Several studies have demonstrated that positive dust anomalies are correlated to SST reduction, a condition unfavorable to hurricane genesis and development, while negative dust anomalies are correlated to SST increment [*Li et al.*, 2004; *Lau and Kim*, 2007; *Foltz and McPhaden*, 2008; *Evan et al.*, 2008; *Wong et al.*, 2008; *Sun et al.*, 2008, 2009]. The response time scales for the ocean (i.e., water) and the air to energy budget changes due to dust are quite different, and the latter is in general much shorter (i.e., months versus days). In this study, our primary interest is the response of air to the energy budget change due to dust-radiation processes, and how this response modifies SAL and environmental vertical shear, which could have an impact on TC genesis and development. To investigate the response and modification, an online tracer model based on the Weather Research and Forecasting (WRF) model [*Skamarock et al.*, 2008] was developed to simulate dust transport and dust-radiation processes. The effects of dust-microphysics interactions were not included in this study, but will be investigated in the near future. The paper is organized as follows. In section 2, satellite observations are used to depict the SAL signature in the atmosphere. The description of the tracer model and numerical design are presented in section 3, and results are discussed in section 4. Concluding remarks are given in section 5.

2. Observed SAL Characteristics From Satellite Data

[8] Although the final goal is to study the impact of dust-radiation interactions on hurricane genesis and intensification, the occurrence of a hurricane during the time period of interest was not a criterion when selecting a case. This is because lasting dust effects might still exist in model initial conditions, even though the dust-radiation effects are deactivated during simulations. A careful design on this type of numerical experiments is required and deserves a separate study. A dust outbreak event that occurred during 18–20 July 2005 was selected for this case study. This case was chosen because (1) the primary interest of this study is to examine the dust-radiation effects on the environmental modification, and (2) a clear dust signature was found on satellite images for this dust outbreak event after looking through months of aerosol optical depth (AOD) satellite data. A clearly defined dust outbreak in AOD retrieval data was important for model development and verification in this study.

[9] Figures 1a and 1b show satellite retrieved 700 hPa temperature and total precipitable water (TPW), respectively, from the Atmospheric Infrared Sounder (AIRS), collected from 1300 UTC to 1700 UTC 20 July 2005. The dry and warm SAL was portrayed by satellite observations quite well qualitatively and spanned about 15–20 degrees in the north-south direction off the coast of northern Africa. After propagating to the ocean, the 700 hPa temperature within SAL was about 4 K warmer than the environment. The maximum

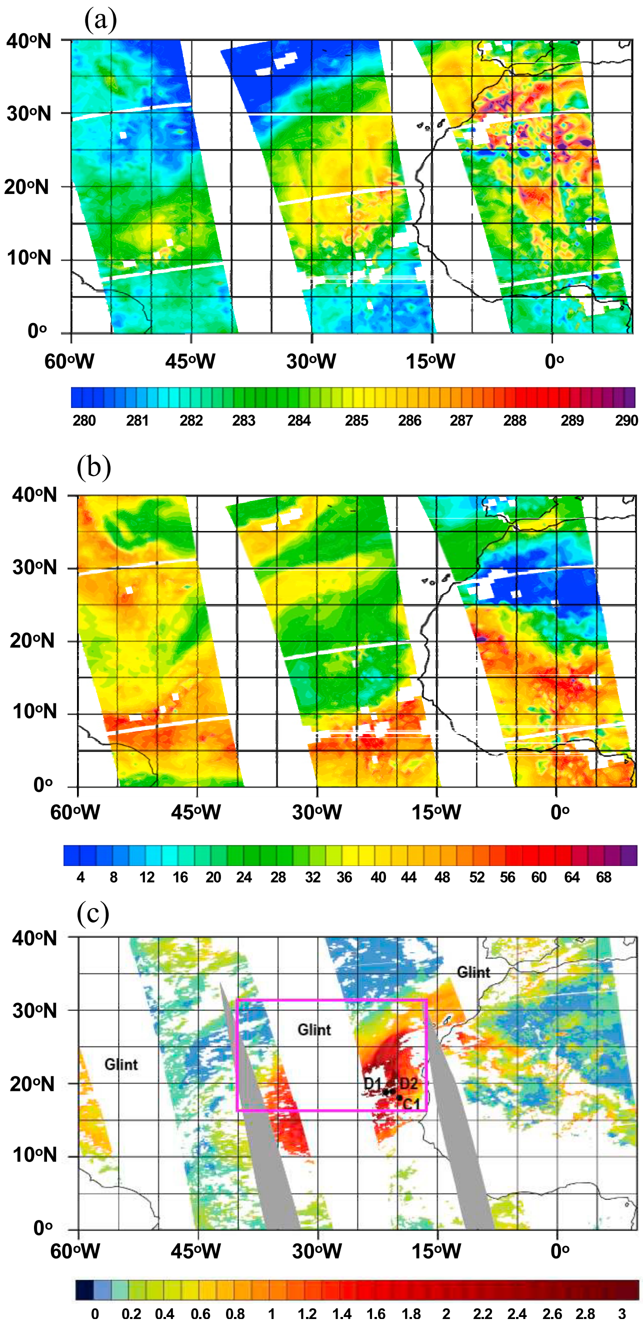

Figure 1. (a) 700 hPa temperature (K) and (b) total precipitable water (TPW, mm) from Atmospheric Infrared Sounder (AIRS), and (c) aerosol optical depth (AOD) from Moderate Resolution Imaging Spectrometer (MODIS) onboard Satellite Aqua. Satellite data were collected approximately from 1300 to 1700 UTC 20 July 2005. In Figure 1c, data over land and ocean are from the deep blue and dark targeting retrievals, respectively. The gray shading indicates gaps between MODIS AOD swaths. The cloudy regions and glint areas (i.e., glints) within 40° of the specular reflection angle were removed in the original data set. D1, D2, and C1 are the locations for vertical temperature profiles in Figure 4. The magenta box covers the same area as the box in Figure 3a.

warm anomaly, relative to the environment, reached 6–7 K. The TPW in dry areas over land was as low as 4 mm and over ocean it was about 40 mm drier than the moist air to the south of SAL. One has to be cautious when using retrieved data over the dusty region as their qualities are in general not good (Figure 2).

[10] Figure 1c shows retrieved aerosol optical depth (AOD) from the Moderate Resolution Imaging Spectrometer (MODIS) at a wavelength of 0.550 μm from around 1300 UTC to 1700 UTC 20 July 2005. Figure 1c is a composite of MODIS Deep Blue products over land [*Hsu et al.*, 2004] and dark targeting products over ocean [*Remer et al.*, 2005]. Within SAL, observed AOD was high over ocean off the coast and relatively small over land. Note that, although AIRS and MODIS are both onboard Aqua, their swath widths (1600 km for AIRS and 2300 km for MODIS) and scanning angles are different. Therefore, the swath in Figure 1c does not overlap exactly with Figures 1a and 1b. In general, aerosols over northern Africa and the eastern Atlantic Ocean are mainly contributed from Saharan dust and sub-Sahelian tropical forest biomass burning. The transport of Saharan dust to the Atlantic Ocean can happen any time of the year,

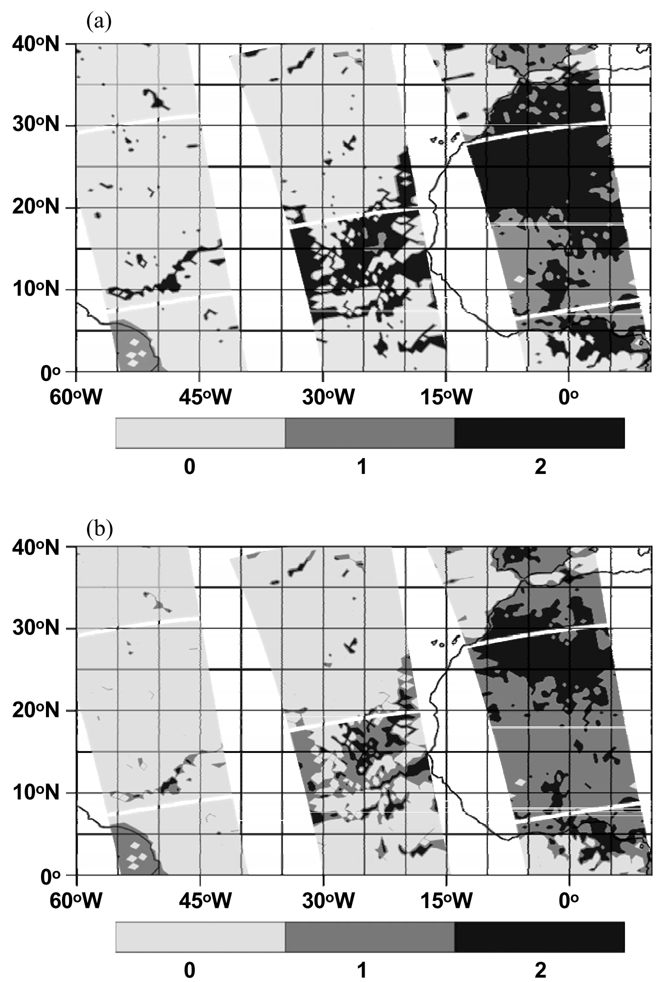

Figure 2. The quality flag plots of AIRS (a) temperature and (b) moisture retrievals corresponding to Figures 1a and 1b, respectively. The light gray color indicates best quality, gray indicates good quality, and black indicates bad quality.

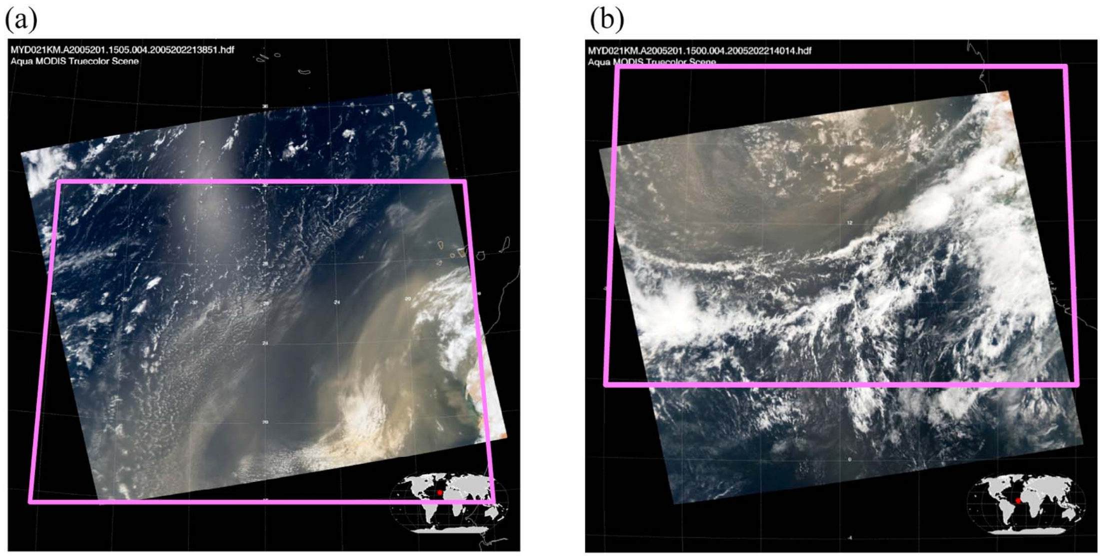

Figure 3. True color satellite images from Aqua MODIS at (a) 1505 UTC and (b) 1500 UTC on 20 July 2005. Figure 3b is located to the south of Figure 3a. The magenta boxes in Figures 3a and 3b correspond to the box in Figure 1c and the plotting area in Figure 13a, respectively.

but is more pronounced during summer, while the biomass burning mainly occurs during winter [*Haywood et al.*, 2008; *Johnson et al.*, 2008; *Léon et al.*, 2009]. Therefore, the high AOD values in Figure 1c indicate the occurrence of a dust outbreak event, which is seen in true color satellite images (Figure 3). High AOD values (i.e., high dust concentration) were located toward the southern half of SAL, with values larger than 1.5. The maximum AOD, which was higher than 3 and reached a maximum of 4 (dark red spots in Figure 1c), approximately coincided with the location of maximum temperature at 700 hPa (i.e., red spots around 15–20°N and 20–25°W in Figure 1a), indicating strong radiation absorption because of high dust concentration.

[11] The AIRS retrieved vertical temperature soundings at three locations close to the highest AOD over ocean (see dots in Figure 1c) were plotted (Figure 4). Soundings from points D1 and D2 were within the extremely dusty region (i.e., AOD ~ 4), while point C1 was located in a relatively clean area (AOD < 1.5), but close to D1 and D2. This ensures that these three air columns originated from a similar environment (i.e., Saharan Desert) and were also exposed to similar solar radiation (i.e., similar zenith angle). The temperature profiles show that heating occurred at columns D1 and D2 from about 900 hPa to 530 hPa. The temperature difference between columns D1 and C1 was greater than that between columns D2 and C1 since column D1 contained more dust (i.e., higher AOD). Column D1 was up to about 3 K warmer than column C1, while its temperature near the surface was cooler by about 6 degrees. Note that the vertical resolution of AIRS soundings is relatively coarse in the lower atmosphere (e.g., the lowest three levels are 1000 hPa, 925 hPa, and 850 hPa).

3. Description of the WRF Tracer (WRFT) Model Development and Experiment Design

3.1. WRFT Development

[12] A tracer model, based on the Advanced Research WRF (ARW) model V3.1.1 [*Skamarock et al.*, 2008], was

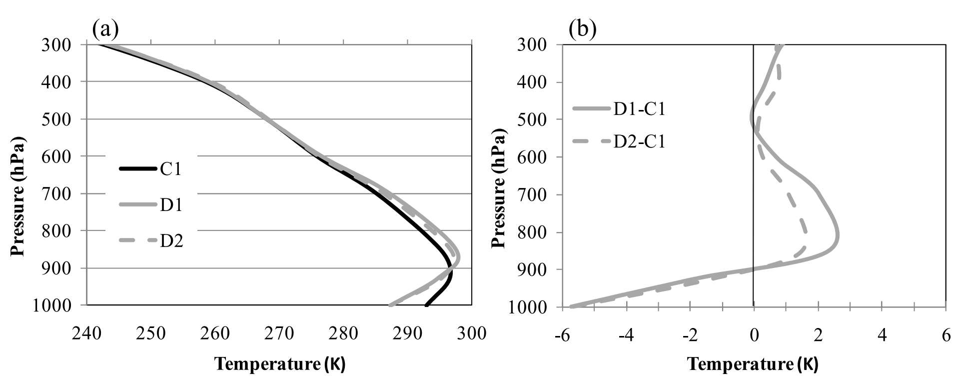

Figure 4. (a) Temperature soundings from AIRS at D1, D2, and C1 in Figure 1c over ocean and (b) the temperature differences of soundings D1 and D2 from C1. Soundings were collected around 1500 UTC 20 July 2005.

Table 1. Estimated Percentage of Sand, Silt, and Clay for Each Soil Type[a]

Soil Types	Percentage (%) Sand	Silt	Clay	Size (μm)	V_T (cm s^{-1})
Sand	100	0	0	50	73
Loamy sand	82	10	8	42	58
Sandy loam	62	28	10	33.9	42
Silt loam	20	65	15	16.6	10
Silt	0	100	0	10	4.4
Loam	40	40	20	24.1	23
Sandy clay loam	60	12	28	31.4	37
Silt clay loam	10	55	35	10.7	5
Clay loam	30	35	35	18.7	12
Sandy clay	50	8	42	26.1	27
Silt clay	8	46	46	8.9	3.5
Clay	0	0	100	0.7	0.018

[a]Based on Figures 3–16 of *Soil Survey Division Staff* [1993]. The sizes and sedimentation speeds (V_T) for pure sand, silt, and clay were estimated from *Tegen and Fung* [1994], while the rest were linearly interpolated from these three types according to their compositions [*Chen et al.* 2008, Table 1].

developed to study the effect of dust-radiation processes on the modification of SAL and its environment, which can potentially influence Tropical Cyclone (TC) genesis and development. Although the WRF chemistry model (WRF-CHEM) can be used for tracer simulations, it requires more memory, as well as some modification. Therefore, a WRF tracer model was developed independently for the study.

[13] WRF is a compressible, nonhydrostatic model, which uses a Runge-Kutta third-order time scheme, high-order advection schemes, the Arakawa C grid, and terrain-following mass coordinates. The model's governing equations are written in flux form, which conserves mass and dry entropy. The calculation of the coupled dust (or tracer) mass was added into the WRF model and the equation is written as:

$$\frac{\partial \mu C}{\partial t} = \nabla \bullet \vec{V}\mu C + C_{pbl} + C_{COV} + S_C + E_C,$$

where C is the dust mixing ratio (kg kg^{-1}), and $\mu(= P_{hs} - P_{ht})$ is the difference of the hydrostatic pressure between the model surface (P_{hs}) and model top (P_{ht}) (i.e., column mass). The symbols S_C, C_{pbl}, C_{Cov}, and E_C represent the dust processes of dust sedimentation, subgrid boundary layer mixing, subgrid cumulus mixing, and source/sink terms, respectively. The major source is the surface dust emission that is inputted into the model's first half layer, and the sink term is the deposition to the ground because of sedimentation. A time splitting method, which allows a smaller time step for the sedimentation calculation, was implemented because of the high vertical spatial resolution near the surface in the model. Wet deposition was ignored and will be added into WRFT in the near future for the dust-microphysics study. There are 12 default types of dust (Table 1) in WRF, which are tracked as individual tracers in WRFT. Similar to the work of *Chen et al.* [2008], the three basic types (i.e., clay, silt, and sand) were based on the work of *Tegen and Fung* [1994], while the rest were roughly estimated from these three basic types (Table 1) according to Figures 3–16 by *Soil Survey Division Staff* [1993]. The sedimentation is calculated using terminal velocities specified in Table 1.

[14] In WRFT, dust emission was controlled by three parameters, as in the work of *Chen et al.* [2008]: the vegetation type, soil moisture, and 10 m wind speed (u_{10}). Dust uptake was assumed to occur only at places where the vegetation type is barren and the soil volumetric moisture is less than 0.2. After satisfying these preconditions, dust emission then takes place when u_{10} is stronger than a threshold (u_{10c}), which was set to 6.5 m s^{-1} in this study. The formula for the surface dust flux, e_C (μg s^{-1} m^{-2}), which is based on the work of *Gillette* [1978] and *Tegen and Fung* [1994], is written as the following:

$$e_C = \max(C(u_{10} - u_{10c})u_{10}, 0),$$

where the dimensional constant, C (μg m^1 s^{-5}), is set to 0.4. Note that the dust distribution at the initial time is ignored (i.e., the model starts integrating without background dust in the atmosphere).

[15] The National Aeronautics and Space Administration (NASA)/Goddard Space Flight Center (GSFC) radiation scheme [*Chou and Suarez*, 1999; *Chou et al.*, 2001], which consists of shortwave and longwave radiation, was used for the examination of the dust-radiation effects. The GSFC longwave scheme was newly implemented into WRFT for this study. The radiation parameterization includes absorption by ozone, water vapor, oxygen, carbon dioxide (CO_2), nitrous oxide (N_2O), methane (CH_4), trichlorofluoromethane (CFC11), dichlorodifluoromethane (CFC12), and chlorodifluoromethane (CFC22), as well as absorption and scattering by clouds, aerosols, and molecules (Rayleigh scattering). For the shortwave calculation, fluxes are integrated from 0.175 to 10 μm, divided into 11 bands (Table 2). For the longwave calculation, fluxes are integrated virtually over the entire spectrum, from 3.33 μm and above, divided into nine bands (Table 2). In WRFT, the aerosol effect because of dust was added into both shortwave and longwave radiation calculations. For a given type of dust, aerosol optical properties (i.e., single-scattering albedo, asymmetry parameter, and extinction coefficient) with respect to different wavelengths were calculated using the Optical Properties of Aerosols and Cloud (OPAC) software package [*Hess et al.*, 1998]. In OPAC, the optical properties for 10 types of aerosols can be calculated using Mie theory and their basic microphysical properties (such as the size distribution and spectral refractive index). Compared to the traditional Mie theory calculation, OPAC has the advantage of lower computational cost, but has less flexibility in input microphysical data. The code has been commonly used in modeling studies to estimate 3-D distributions of aerosol optical properties for particular aerosol types [*Wang et al.*, 2007, 2009; *Chin et al.*, 2009]. In this study, microphysical properties of Saharan dust were considered as those for mineral aerosols with three modes in OPAC (i.e., nucleation, accumulation, and coagulation modes). Therefore, the 12 types of dust in WRFT were roughly lumped into these three modes when calculating optical properties for each of the shortwave and longwave bands, which were stored in look-up tables (Table 2).

Table 2. Optical Properties, Single-Scattering Albedo (ω), Asymmetry Parameter (g), and Extinction Coefficient (σ) of Mineral Dust Aerosols for Shortwave Radiation and Longwave Radiation Used in This Study[a]

	Mineral (Nucleation Mode)			Mineral (Accumulation Mode)			Mineral (Coagulation Mode)		
Wavelengths (μm)	ω	g	σ	ω	g	σ	ω	g	σ
Shortwave Radiation									
0.175–0.225	0.80	0.73	1.027E-04	0.58	0.90	2.807E-03	0.55	0.95	7.559E-02
0.225–0.245	0.80	0.73	1.027E-04	0.58	0.90	2.807E-03	0.55	0.95	7.559E-02
0.245–0.260	0.80	0.73	1.027E-04	0.58	0.90	2.807E-03	0.55	0.95	7.559E-02
0.280–0.295	0.80	0.73	1.027E-04	0.58	0.90	2.807E-03	0.55	0.95	7.559E-02
0.295–0.310	0.84	0.72	9.980E-05	0.61	0.88	2.855E-03	0.55	0.95	7.596E-02
0.310–0.320	0.84	0.72	9.980E-05	0.61	0.88	2.855E-03	0.55	0.95	7.596E-02
0.325–0.400	0.89	0.70	9.532E-05	0.68	0.83	2.905E-03	0.55	0.95	7.631E-02
0.400–0.700	0.97	0.66	7.104E-05	0.88	0.73	3.105E-03	0.67	0.90	7.759E-02
0.700–1.220	0.98	0.61	3.262E-05	0.94	0.69	3.425E-03	0.78	0.84	8.004E-02
1.220–2.270	0.95	0.52	1.080E-05	0.95	0.69	3.334E-03	0.79	0.80	8.392E-02
2.270–10.00	0.50	0.26	8.134E-07	0.89	0.66	1.304E-03	0.80	0.77	9.596E-02
Longwave Radiation									
3.33–5.26	0.00	0.05	2.20E-06	0.15	0.35	5.58E-04	0.42	0.75	7.44E-02
5.26–7.25	0.82	0.32	1.13E-06	0.96	0.67	1.82E-03	0.88	0.74	9.45E-02
7.25–8.23	0.12	0.20	1.30E-06	0.66	0.65	9.15E-04	0.64	0.84	9.31E-02
8.23–9.09	0.01	0.14	1.41E-06	0.28	0.63	4.13E-04	0.54	0.91	6.62E-02
9.09–10.20	0.01	0.11	4.21E-06	0.15	0.54	8.41E-04	0.40	0.88	6.88E-02
10.20–12.50	0.12	0.16	2.82E-06	0.46	0.34	2.06E-03	0.53	0.67	9.77E-02
12.50–18.52	0.04	0.12	1.53E-06	0.50	0.47	9.11E-04	0.54	0.73	9.75E-02
18.52–29.41	0.01	0.05	1.55E-06	0.28	0.22	6.74E-04	0.48	0.51	9.61E-02
>29.41	0.00	0.02	8.38E-07	0.13	0.19	2.36E-04	0.44	0.46	7.26E-02

[a]The σ is normalized at a number density of 1 particle cm^{-3}.

3.2. Experiment Design

[16] The dust outbreak event that occurred around 18–20 July 2005 was chosen for the case study; the reasons for this choice were briefly mentioned earlier. Two domains with resolutions of 27 km and 9 km (figure not shown) and two-way interaction were configured. The number of grid points for domains 1 and 2 in the x-y-z directions were 491 × 331 × 31 and 751 × 571 × 31, respectively. The initial and boundary conditions were from the Global Forecast System (GFS) reanalysis, which has a temporal resolution of 6 h and a spatial resolution of 1° × 1°. The Purdue microphysics parameterization [*Chen and Sun*, 2002], Medium Range Forecast (MRF) boundary layer parameterization [*Hong and Pan*, 1996], Kain-Fritsch (KF) cumulus parameterization [*Kain*, 2004], and GSFC shortwave and longwave radiation parameterization [*Chou and Suarez*, 1999; *Chou et al.*, 2001] were used for all numerical simulations. Dust mixing due to boundary mixing and cumulus convection were taken into account in MRF and KF schemes, respectively. The fifth-order advection scheme for the horizontal direction and the third-order for vertical were chosen. The WRFT model integrated for 4 d, starting from 0000 UTC 18 July 2005, and the time step for domain 1 was 120 s. During the model integration, free atmosphere (i.e., above the boundary layer) in domain 1 was nudged to reanalysis using four dimensional data assimilation (FDDA) to prevent drifting of large-scale patterns.

[17] Two numerical experiments were conducted. Both numerical settings, including dust simulation, were the same except that one had dust-radiation interaction activated (named ON) and the other had the dust-radiation interaction deactivated (named OFF). The sea surface temperature (SST) in both WRFT simulations was updated using 6 hourly GFS reanalysis. The model started emitting dust from the surface whenever the criteria, i.e., vegetation type, soil moisture, and 10 m wind, were satisfied. There was no dust at the model initial time.

4. Simulation Results and Discussion

4.1. SAL, Dust, and Radiation Budget

[18] Figures 5a and 5b show simulated 700 hPa temperature and wind vectors, and total precipitable water (TPW), respectively, from OFF at 1500 UTC 20 July 2005 after a 63 h integration, at the time when satellite data were available and also when the dust plume propagated to the eastern Atlantic ocean. OFF was able to reproduce SAL's general features (i.e., dry and warm) without including the dust-radiation effects. Simulated temperatures were comparable to satellite retrievals within SAL and its environment to the south of SAL (Figure 1). However, the simulated maximum temperature anomaly within SAL was shifted northwestward and was about 2 K colder (Figure 5a versus Figure 1a). Simulated TPW within SAL and its environment were also comparable to satellite retrievals; the simulation produced extremely dry air over the desert, a dry tongue within the SAL, another dry zone to the north of SAL, and very moist air in the convective zone (Figures 5b versus Figure 1b). Over land a moist band oriented in the northwest-southeast direction, north of 15°N, was found from TPW AIRS retrievals (Figure 1b); a similar moist band was also found from MODIS near Infrared TPW retrievals (figure not shown). However, this was not shown in either the OFF (Figure 5b) or the ON simulation. Because of the thermal wind balance, a Middle Level Easterly Jet (MLEJ) was simulated at the boundary of the warmer Saharan air to the north and cooler air to the south (i.e., a baroclinic zone).

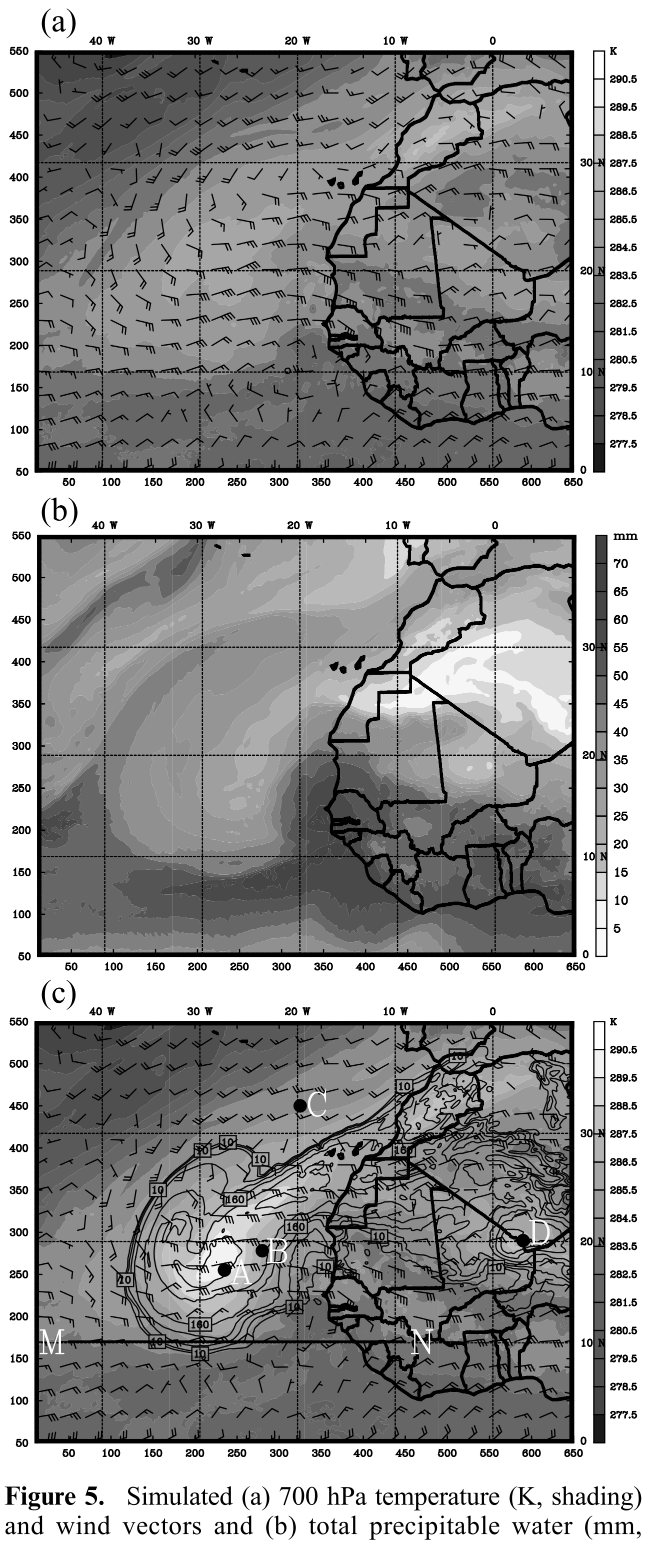

Figure 5. Simulated (a) 700 hPa temperature (K, shading) and wind vectors and (b) total precipitable water (mm, shading) at 1500 UTC 20 July 2005 (63 h simulation) from experiments conducted without the dust-radiation effects (OFF). (c) The same as Figure 5a except from experiments conducted with and the dust-radiation effects (ON) plus simulated column integrated dust in contours ($\times 10^4$ μg m^{-2}). In Figure 5c, dots with letters A to D are the locations for vertical soundings plotted in Figure 8, and the thick black line MN is the location of the vertical cross-section plots in Figures 17 and 18.

[19] The dust outbreak was reproduced from ON (Figure 5c), as well as from OFF. The dust plume propagated from the Sahara Desert into the eastern Atlantic Ocean and was located slightly toward the southern half of SAL, similar to satellite retrievals (i.e., the location of high AOD). The maximum temperature location from ON was slightly shifted southeastward, which matched the satellite observations (Figure 1c) better than in the OFF simulation, because of the correction from the dust-radiation interaction (i.e., heating). However, the maximum temperature from ON was warmer than AIRS satellite retrievals (about 2 K). This can be partially explained by the difference of spatial resolutions (i.e., 9 km for model simulation versus 45 km for AIRS temperature retrievals). However, the errors from the treatment of dust characteristics and optical properties (e.g., single-scattering albedo and asymmetry), simulated wind, dust amount and vertical distribution, and satellite retrievals (i.e., poor quality over dusty region; see Figures 1a and 2a) can also contribute to increased temperature in simulations. In particular, the shortwave absorption (reflection) by dust might be overestimated (underestimated), as has been reported in recent studies and discussed in the introduction [*Colarco et al.*, 2002; *Sinyuk et al.*, 2003].

[20] Figure 6 shows simulated dust in horizontal and vertical cross sections from ON. Over the desert, heavy dust was pumped into the atmosphere and deeply mixed within the boundary layer during the daytime on 1800 UTC 18 July 2005 (Figures 6a and 6b). Because of inhomogeneous winds at different levels, the dust plume at higher levels (e.g., 700 hPa) propagated faster than at lower levels (e.g., 950 hPa) because of the MLEJ. The separation of the plumes' leading edges at these two levels became larger over time. When the dust plume propagated away from Africa, it was located between two troughs that were about 2000–3000 km apart (Figure 6). The maximum dust concentration was around the ridge region and primarily located to the north of the jet. These features are similar to those described in the three-dimensional Saharan dust plume conceptual model by *Karyampudi et al.* [1999]. Later in the simulation, the dust plume at 700 hPa curved to the south and north, as shown in Figure 6e (96 h simulation), because of an African easterly wave disturbance (i.e., cyclonic circulation) to the south of SAL and an anticyclonic eddy to the north, respectively (winds not shown). In vertical cross sections, a group of local maxima of simulated dust concentration was trapped close to the surface because of the inversion and sedimentation. A second group of local maxima between about 700 to 500 hPa (Figures 6d and 6f) was due to deep boundary layer mixing over the source region, upward advection by the buoyancy (i.e., dust-radiation interaction), and faster advection by the jet in the middle levels. Sixty-three hour simulated AOD at the 0.55 μm wavelength (shortwave) is shown in Figure 7a. Overall, the value over the dust plume region was about 1.5 to 2.0, which is comparable to retrieved satellite data (Figure 1c). However, the simulated maximum value (~2.1) was much smaller than the value retrieved from satellite data (i.e., AOD > 3), which might be overestimated. From the satellite image in Figure 3a, it can be seen that a cloud existed underneath the dust plume over the extreme high AOD region, and this might have contaminated the AOD retrieval [*Kaufman et al.*, 2005; *Zhang et al.*, 2005; *Redemann et al.*, 2009]. Note that this cloud was most

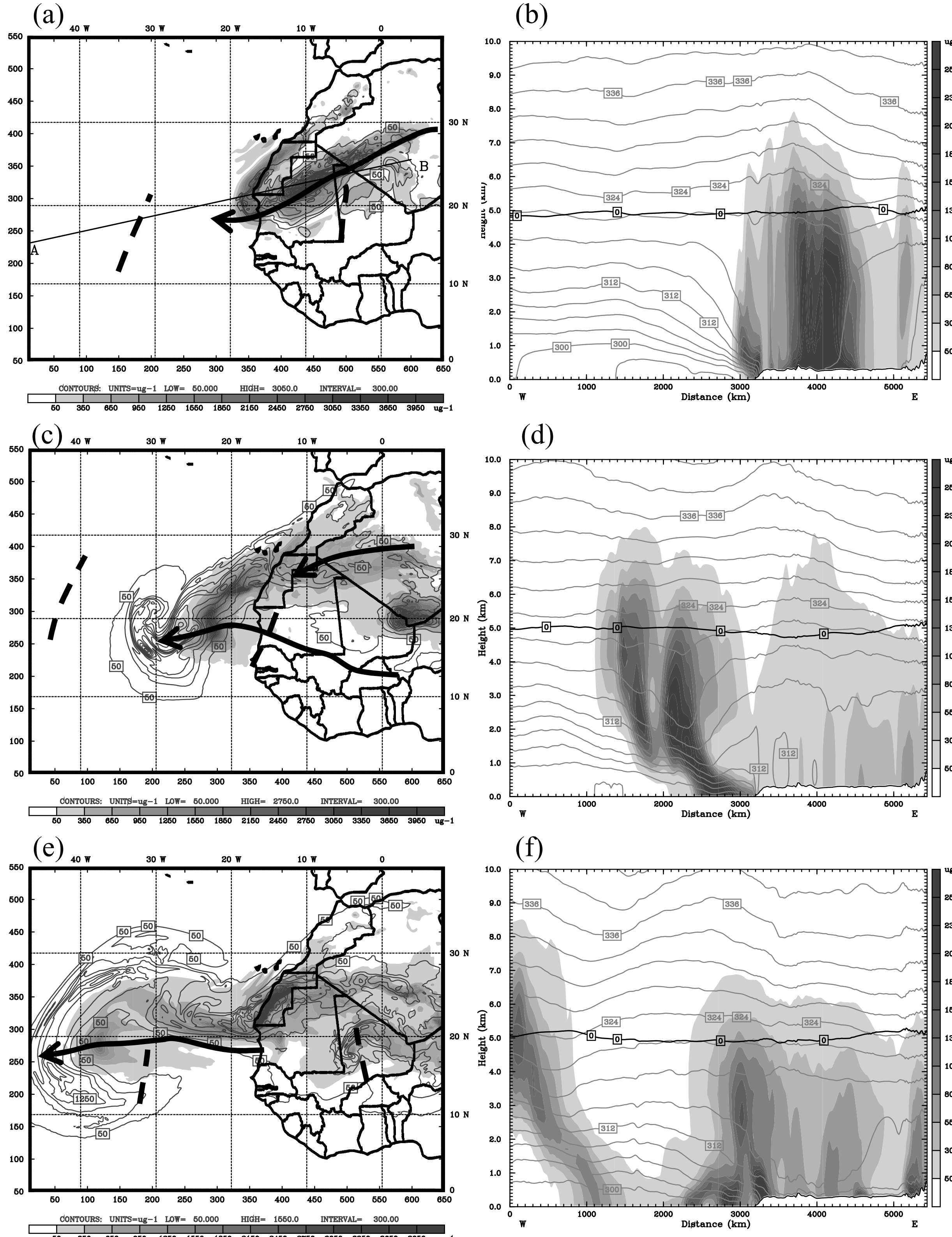

Figure 6. Simulated total dust mixing ratio (μg kg^{-1}) at 950 hPa (shading) and 700 hPa (contour lines) after (a) 18 h (1800 UTC 18 July), (c) 60 h (1200 UTC 20 July), and (e) 96 h (0000 UTC 22 July) integrations and simulated vertical cross sections of total dust mixing ratio (shading) and potential temperature (contour lines) with an interval of 3 K, along the line AB in Figure 6a, after (b) 18 h, (d) 60 h, and (f) 96 h integrations from ON. The thick arrows and dashed lines in Figure s 6a, 6c, and 6e represent the 700 hPa jet and trough locations, respectively. The solid black lines in Figures 6b, 6d, and 6f are the freezing level.

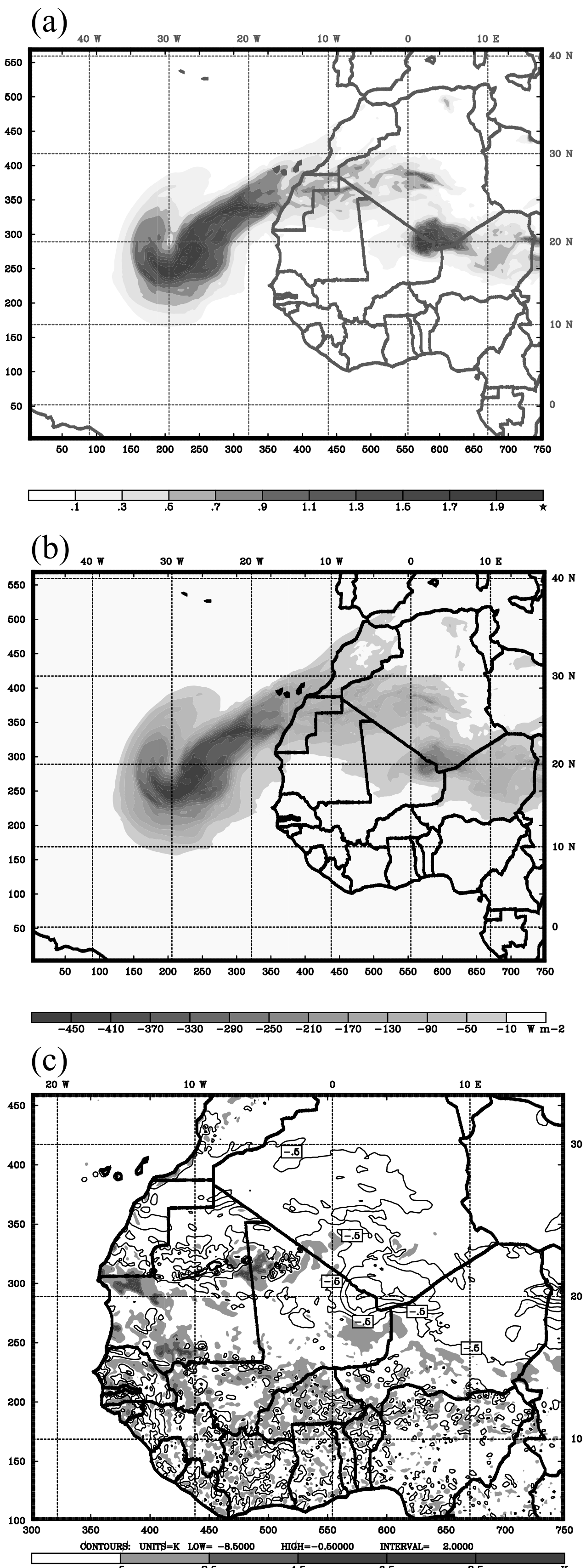

likely located at the top of the boundary layer because the air above (i.e., SAL) was very dry. The simulated AOD due to dust was much smaller over land than over ocean, which is consistent with MODIS AOD retrievals (Figure 1c), except that a large value was simulated at the border of Algeria, Mali, and Niger, where the satellite AOD was missing. For long-wave bands, simulated AOD values due to dust were generally comparable to those from shortwave radiation (figure not shown).

[21] The suspended high-concentration dust significantly reduced the downward shortwave radiation during the daytime. Absorption and reflection by suspended dust reduced the clear-sky downward shortwave radiation by more than 400 W m^{-2} at the surface (Figure 7b), which cooled the surface temperature by up to 9 K (i.e., at the border of Chad and Sudan in Figure 7c). Over the ocean, since a lower boundary condition was imposed using GFS data, there was no difference in the sea surface temperature between ON and OFF.

4.2. Temperature, Moisture, and Wind

[22] The skew-T log-P diagrams of 60 h simulated soundings at 1200 UTC 20 July 2005 with and without dust-radiation effects were compared at four different sites (Figure 8). The enhanced pre-existing trade wind inversion because of warm SAL above is clearly shown in soundings A, B, and C. The first two soundings were exposed to a dusty environment. In particular, sounding A was located in the area of high column-integrated dust. Therefore, the temperature, as well as moisture, modification of this sounding due to dust-radiation effects was more significant. When compared to their counterparts without the dust-radiation interaction, soundings A and B from ON became warmer, except at the layer above the SAL (~100 hPa in depth) due to adiabatic cooling from the upward motion (or the adiabatic cooling was larger than the dust heating if there was dust). The weak warming within the boundary layer in sounding A was due to dust-longwave radiation interaction (discussed more later). Both columns A and B became more moist and a similar condition was seen in satellite retrieved TPW as well (around 28°W and 18°N in Figure 1b). Sounding C was located within SAL, but in a clean environment, and had almost no difference in temperature and moisture profiles between ON and OFF. For sounding D over the desert, the lower atmosphere was dry and the mixed boundary layer was deep, resulting from the strong sensible heat flux. The inclusion of dust-radiation effects increased the temperature in the boundary layer because of heating from dust-radiation interactions, which overcame the reduction of the sensible heat flux from the cooled surface (i.e., boundary layer parameterization; figure not shown).

Figure 7. (a) Simulated aerosol optical depth at the wavelength of 0.55 μm due to dust from ON, and the differences of (b) the clear-sky downward shortwave radiation (W m^{-2}) due to dust at the surface and (c) the surface temperature difference (K, positive shading and negative contour lines) between ON and OFF (ON–OFF) at 1500 UTC 20 July 2005 after a 63 h integration. For contour lines in Figure 7c, the interval is 2 K and the maximum plotted value is −0.5 K.

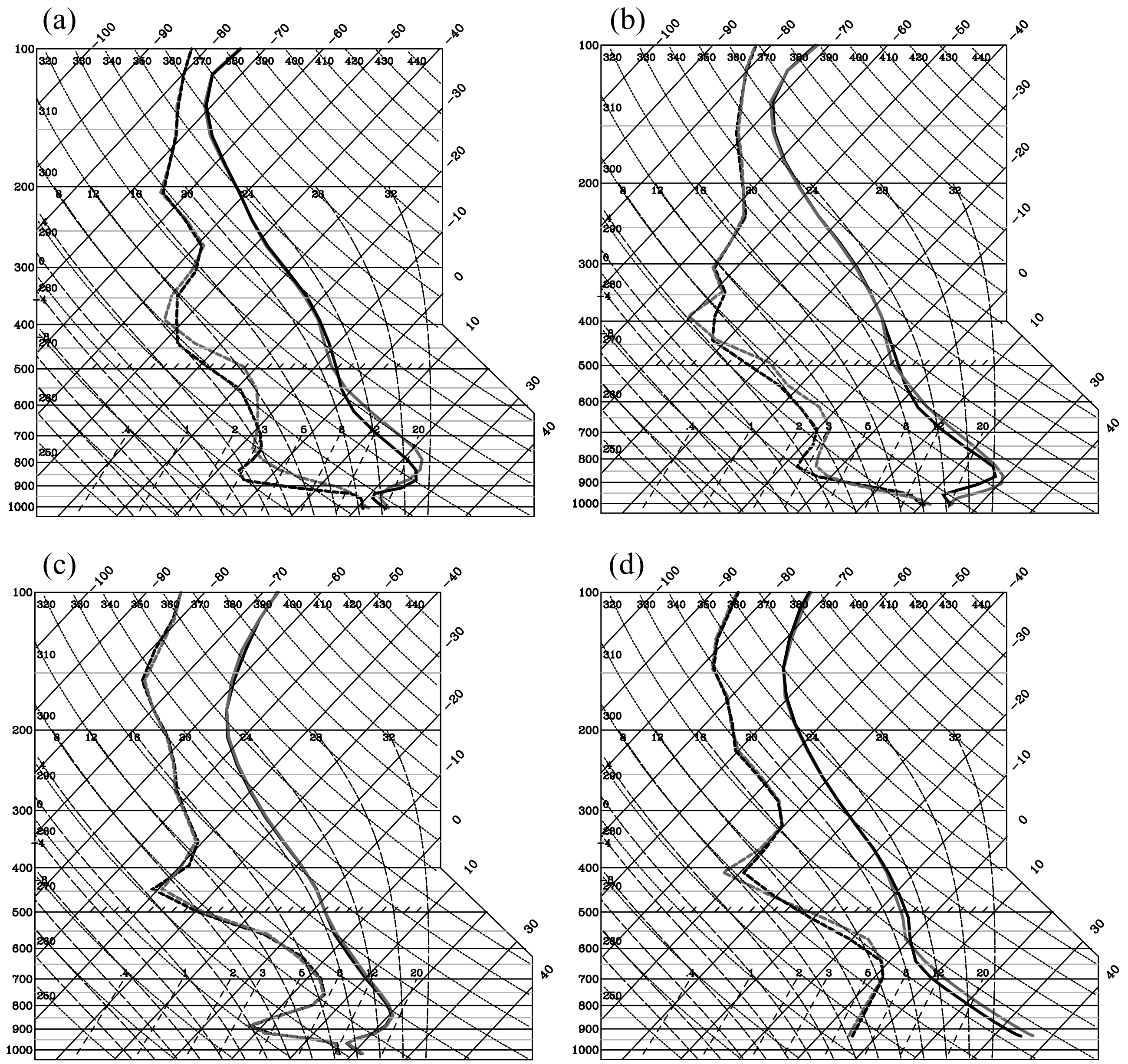

Figure 8. Simulated vertical soundings from ON (gray thick lines) and OFF (black thick lines) at the locations of (a) A, (b) B, (c) C, and (d) D in Figure 5c after a 60 h simulation (i.e., at 1200 UTC 20 July 2005).

[23] Figures 9 and 10 show the horizontal cross sections of temperature differences between simulations with and without the inclusion of dust-radiation effects (ON–OFF) at different pressure levels and with different types of dust-radiation interactions. To help understand the contribution from dust-shortwave and dust-longwave processes, two more numerical experiments were performed. Both configurations were the same as OFF, except that one had dust-shortwave radiation activated (named SON) and the other had dust-longwave radiation activated (named LON). At 600 and 700 hPa levels with both longwave and shortwave interactions, the air was heated (Figures 9c and 9d) since the dust shortwave absorption dominated longwave cooling (Figure 10b versus Figure 10d). The heating/cooling effect, however, became complicated in the lower troposphere, in particular in the boundary layer (Figures 9a and 9b). In general, dust concentration had its maximum near the surface over the source region (i.e., land), while it became quite different over ocean because of the inhomogeneity of wind in both horizontal and vertical directions (Figure 6; i.e., maximum in the lower to middle troposphere, shift of the dust plumes at different levels, etc.). Within the boundary layer over ocean, competition between the absorption heating, extinction cooling, emission cooling, and adiabatic heating/cooling made the net heating/cooling effect more complex (Figures 9a and 9b), in particular for dust-shortwave interaction from SON (Figure 10a). It is interesting to see that within the boundary layer where the dust plume was located

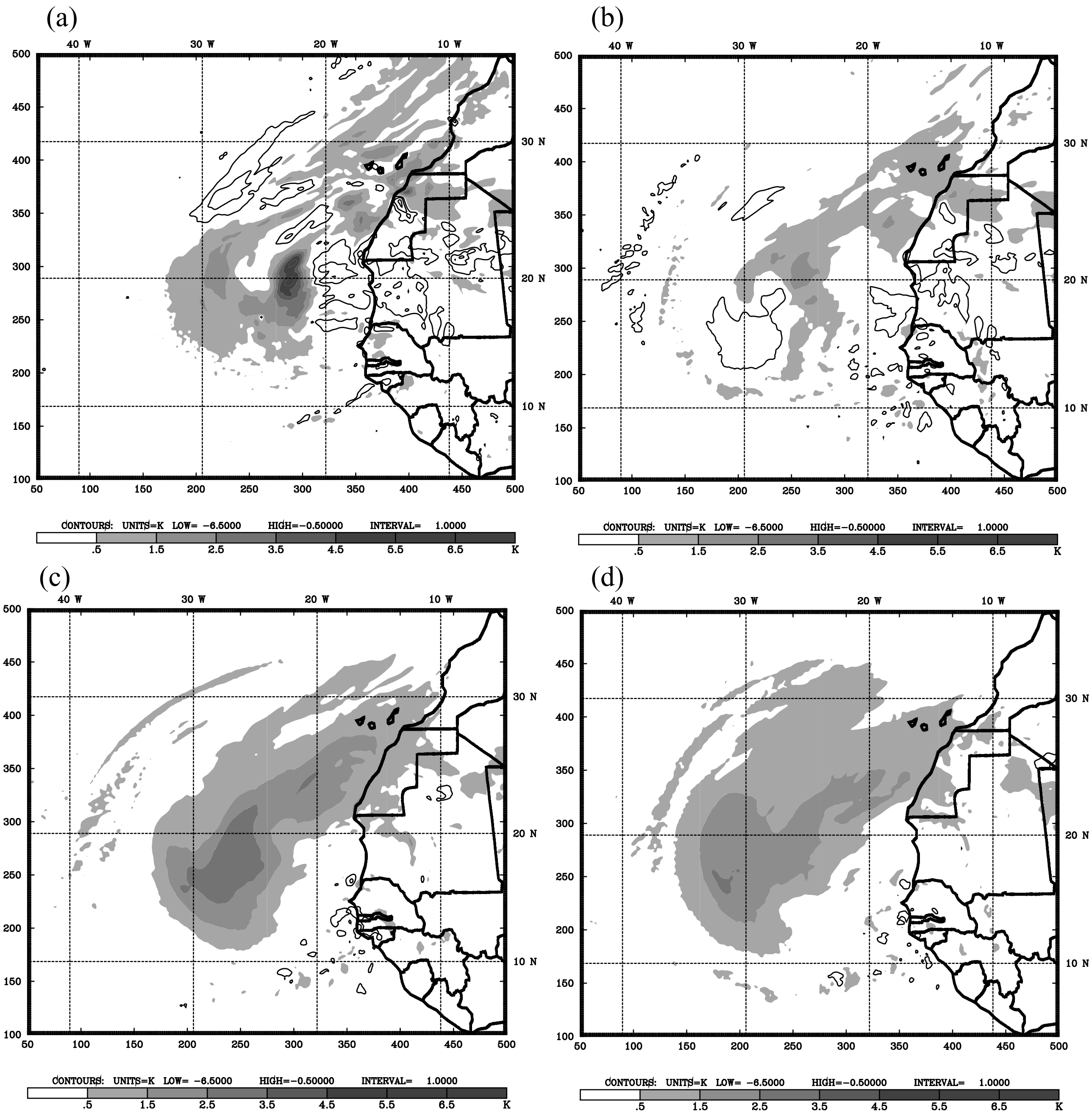

Figure 9. Simulated temperature difference (K) between ON and OFF (ON–OFF) at (a) 950 hPa, (b) 850 hPa, (c) 700 hPa, and (d) 600 hPa at 1200 UTC 20 July 2005 after a 60 h simulation. Shading (contour lines) indicate positive (negative) values. The contour interval is 1 K.

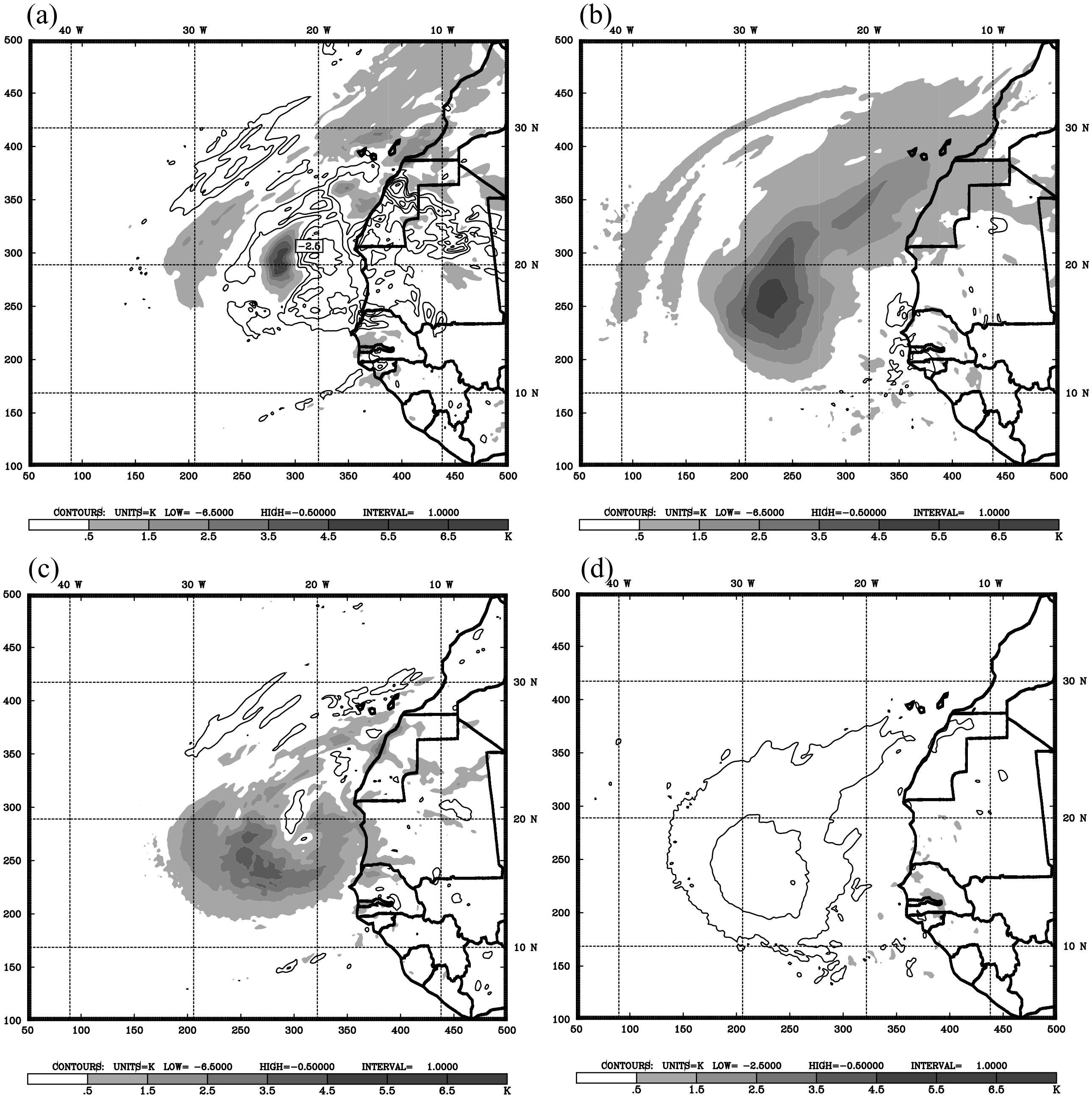

Figure 10. Simulated temperature difference (K) between dust-shortwave radiation activated (SON) and OFF (SON–OFF) at (a) 950 hPa and (b) 700 hPa at 1200 UTC 20 July 2005 after a 60 h simulation. (c) and (d) are the same as (a) and (b), respectively, except for the difference between dust-longwave radiation activated (LON) and OFF (LON–OFF). Shading (contour lines) indicate positive (negative) values. The contour interval is 1 K.

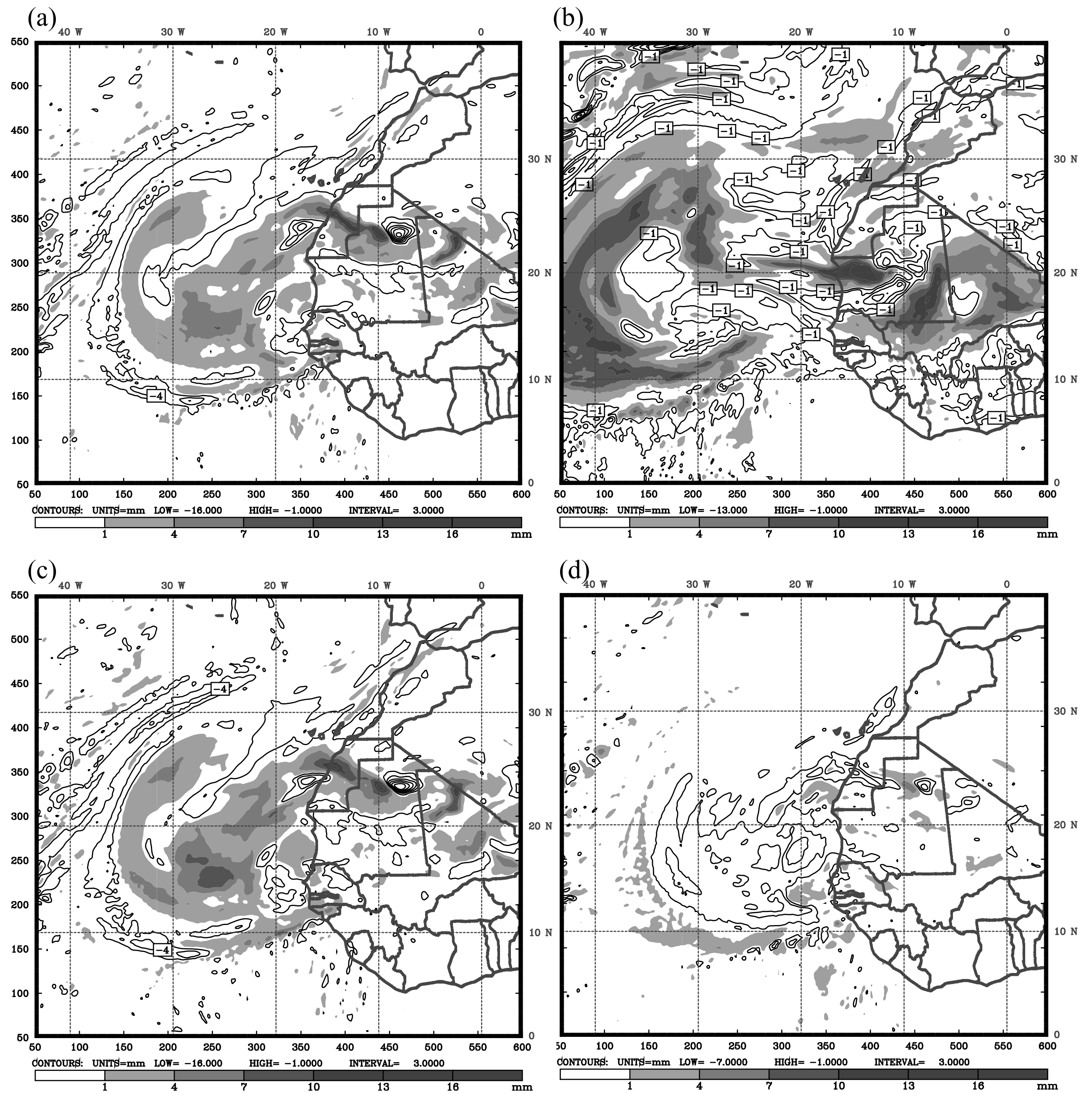

Figure 11. Simulated total precipitable water difference (mm) between ON and OFF (ON–OFF) after (a) 60 h (1200 UTC 20 July 2005) and (b) 96 h integrations (0000 UTC 22 July 2005). (c and d) Same as Figure 11a after a 60 h integration, except for the difference between SON and OFF (SON–OFF) and between LON and OFF (LON–OFF), respectively. Shading (contour lines) indicate positive (negative) values. The contour interval is 3 mm.

aloft because of a stronger advection, a net heating was obtained after including dust-radiation interactions (Figure 9a). This is because the downward longwave heating from dust emission aloft dominated the extinction cooling by dust-shortwave absorption and reflection (Figure 10a versus Figure 10c), which is consistent with what was found previously [*Carlson and Benjamin*, 1980; *Zhu et al.*, 2007; *Wong et al.*, 2009]. The domination of the dust-longwave heating over the dust-shortwave cooling decreased with height and was reversed at 850 hPa (around 30°W and 15°N in Figure 9b). Close to the top of the SAL (about 400–500 hPa; figure not shown), a cold temperature anomaly was found because of the adiabatic cooling from the upward motion.

[24] In addition to the direct effects from dust-radiation interaction, the adjustment of temperature profiles could also be contributed from the change of water vapor, a greenhouse gas. Figures 11a and 11b show the difference in TPW

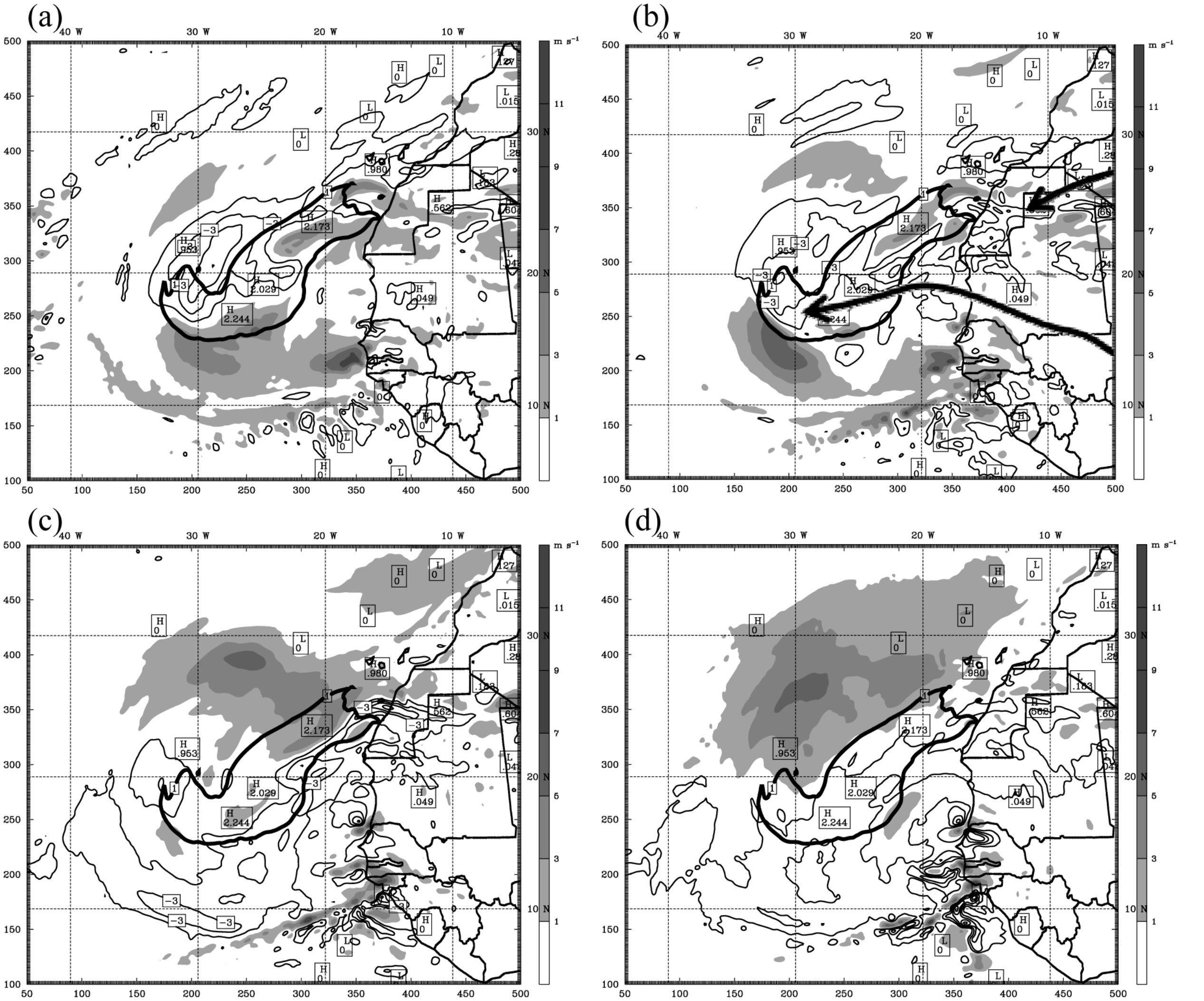

Figure 12. Difference in the east-westerly wind component (m s^{-1}) between ON and OFF (ON–OFF) at (a) 800 hPa, (b) 700 hPa, (c) 600 hPa, and (d) 500 hPa at 1200 UTC 20 July 2005 (60 h simulation). Shading (contour lines) indicates positive (negative) values. The contour interval is 2 m s^{-1}. The thick solid line indicates the constant AOD value of 1.0. The arrows in Figure 12b indicate the locations of jets at 700 hPa.

between ON and OFF (ON–OFF) after 60 h and 96 h integrations, respectively. The dust-radiation interaction resulted in positive TPW anomalies in most of the dusty region with maximum moisture anomalies below 700 hPa (figure not shown). This was mainly contributed from the dust-shortwave radiation interaction, which was slightly offset by the dust-longwave radiation effects (Figure 11c versus Figure 11d). The increase of TPW within SAL enhanced the warming effect by dust-radiation interactions, creating a positive feedback. Note that this positive TPW anomaly is different from what was discussed by *Wong et al.* [2009], who compared averaged moisture variation between columns with different AOD (i.e., dusty versus less dusty columns) within the same region. They found that air columns with a higher AOD were associated with a dry anomaly, which maintained the lower-tropospheric temperature inversion in SAL. The present study investigated the feedback of dust-radiation effects on the moisture modification, which is a secondary effect on the radiation budget (i.e., temperature change through longwave absorption).

[25] The direct and indirect effects of the dust-radiation interaction modified the radiation budget and resulted in the change of temperature profiles in the dusty SAL region. The change in temperature profiles altered the horizontal temperature gradient, which in turn induced the adjustment of the vertical shear (i.e., the change of the horizontal wind) within SAL and its surroundings. Figure 12 shows horizontal cross sections of the zonal wind difference at different pressure levels between ON and OFF (ON–OFF) after a 60 h integration. It is worth mentioning that the dust plume (or area of maximum AOD) was mainly located to the north of the MLEJ (thick arrow in Figure 12) and close to the southern half of SAL. The African monsoon convergence zone as well as an easterly wave disturbance existed off the

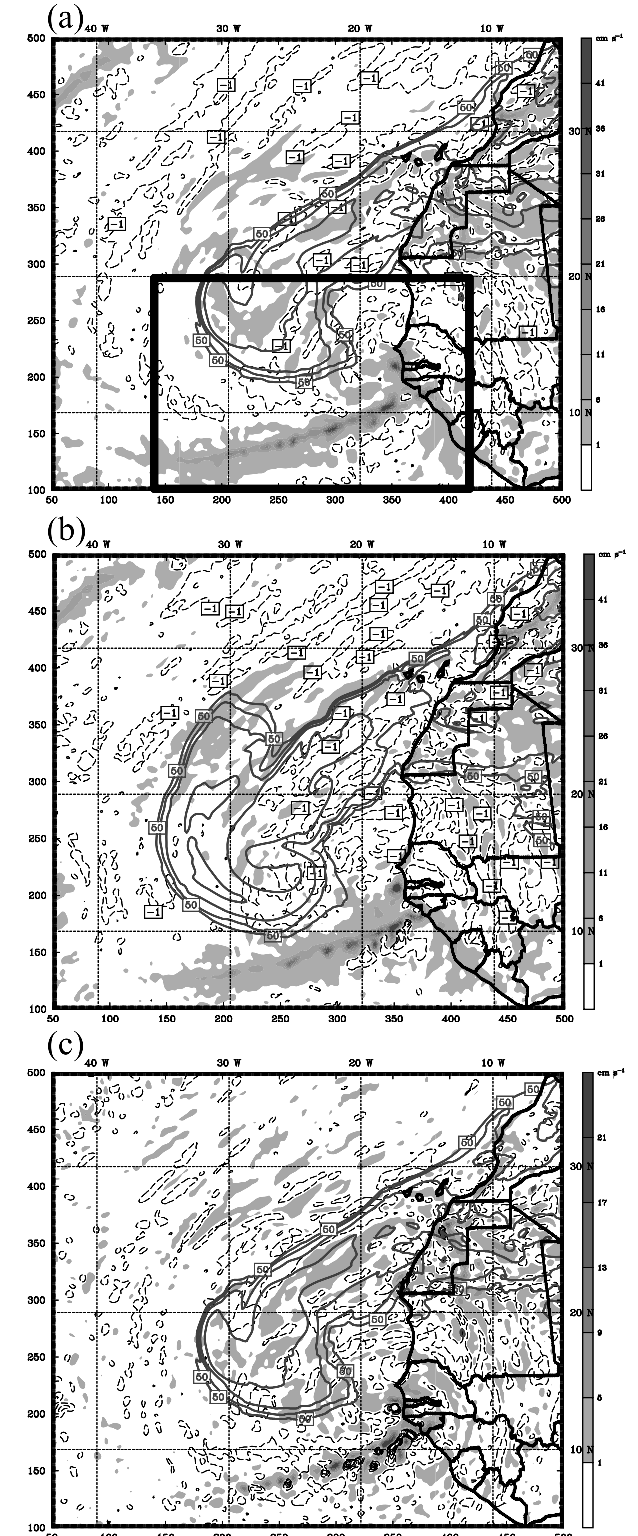

Figure 13. Vertical velocity (cm s^{-1}) and total dust mixing ratio (μg kg^{-3}, solid contour lines) at 800 hPa from (a) ON and (b) OFF at 1200 UTC 20 July 2005 (60 h simulation). (c) Difference of the vertical velocity between them (ON–OFF) plus the total dust mixing ratio from ON. Gray shaded (dashed lines) indicate upward (downward) motion. The black box in Figure 13a covers the same area as the box in Figure 3b.

southwestern coast of northern Africa where the wind increment patterns were more complicated. Over the ocean to the south of SAL (or to the south of the MLEJ), the inclusion of dust-radiation effects made the easterly wind component decrease from the lower troposphere to about 650 hPa (Figures 12a and 12b) and increase from about 650 hPa to 500 hPa (Figures 12c and 12d), indicating an increase of the vertical shear between the lower free atmosphere and the middle troposphere. Results are reversed on the other side (i.e., north) of the maximum dust concentration.

4.3. Vertical Velocity, Static Stability, and Vertical Shear

[26] Figures 13a and 13b show 60 h simulated vertical velocities and the total dust mixing ratio at 800 hPa from ON and OFF, respectively. An organized monsoon convergence zone to the south of SAL was produced by both ON and OFF experiments, and this matched the cloud system observed from satellite very well (see Figure 3b). It was noticed that the strength of the convective system over the monsoon convergence zone was modified by the dust-radiation effects (Figure 13c). While this is an interesting phenomenon, it is beyond the scope of this study. For the ON experiment, another weaker, but also organized, rising zone over the ocean within the dust plume was simulated because of the dust absorption (Figures 13a and 13c). As a result, dust could reach up to an altitude of 8–9 km after a 96 h integration (Figure 6f), which is similar to what was discussed by *Liu et al.* [2003]. It is interesting to see that there were waves propagating outward from the dust plume (Figure 13a) because of diurnal heating from the solar radiation.

[27] The horizontal cross sections of 60 h simulated static stability at different pressure levels from OFF were plotted (Figures 14a–14c). In the lower atmosphere, the boundary layer was well mixed in the middle of the day over the desert, in particular near the surface because of the strong sensible heat flux. Therefore, the static stability over the region was close to zero, or sometimes slightly negative (i.e., super-adiabatic lapse rate) at some spots near the surface (figure not shown). Over the ocean off the coast of northern Africa, the atmosphere was close to neutral within the mixed boundary layer (figure not shown) and the air directly above the boundary layer under SAL was quite stable (i.e., the inversion layer). The altitude of the inversion layer increased from the coast to the dust front (Figure 14a). At 700 hPa and above, the static stability within SAL was still small, while that outside SAL was larger (Figures 14b and 14c). The inclusion of dust-radiation effects increased static stability in most of the dust plume region from the lower troposphere to the maximum heating level, ~600–700 hPa (Figures 14d and 14e), the layer where the temperature lapse rate was decreased (see Figures 9b and 9c). This can suppress the dust mixing in the lower free atmosphere. In contrast, the atmosphere became more unstable from the maximum heating level to the middle troposphere (Figures 14f), which can promote dust mixing.

[28] Dust-radiation effects, such as the change of horizontal wind profiles (Figures 12) and static stability (Figures 14d–14f), and the induced net upward/downward motion (Figure 13c), can modify the dust distribution. Simulated dust from OFF could not reach 500 hPa and detrained below

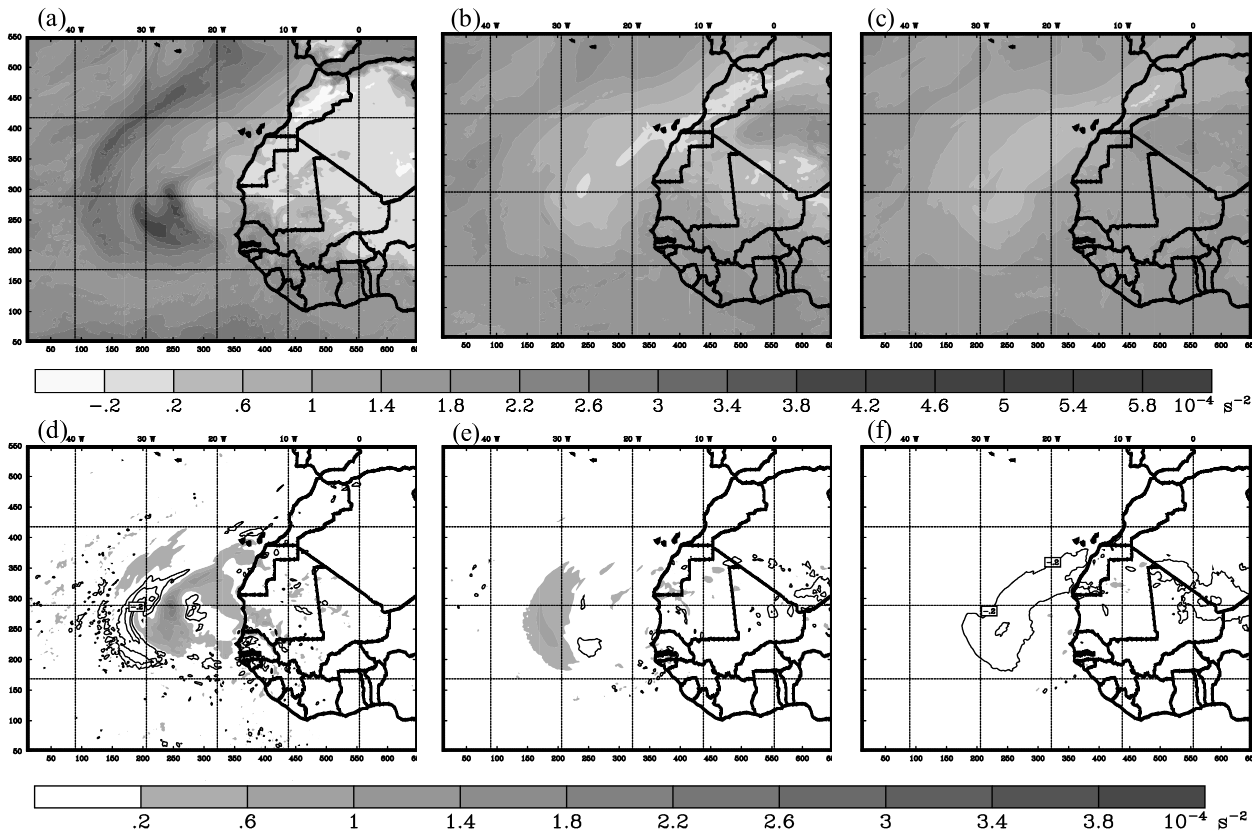

Figure 14. Static stability ($\times 10^{-4}$ s^{-2}) at (a) 850 hPa, (b) 700 hPa, and (c) 600 hPa from OFF at 1200 UTC 20 July 2005 (60 h simulation). (d, e, and f) Same as Figures 14a, 14b, and 14c, respectively, except that they present the difference between ON and OFF (ON–OFF). In difference fields, positive values are shaded and negative are contoured with an interval of 0.4×10^{-4} s^{-2}.

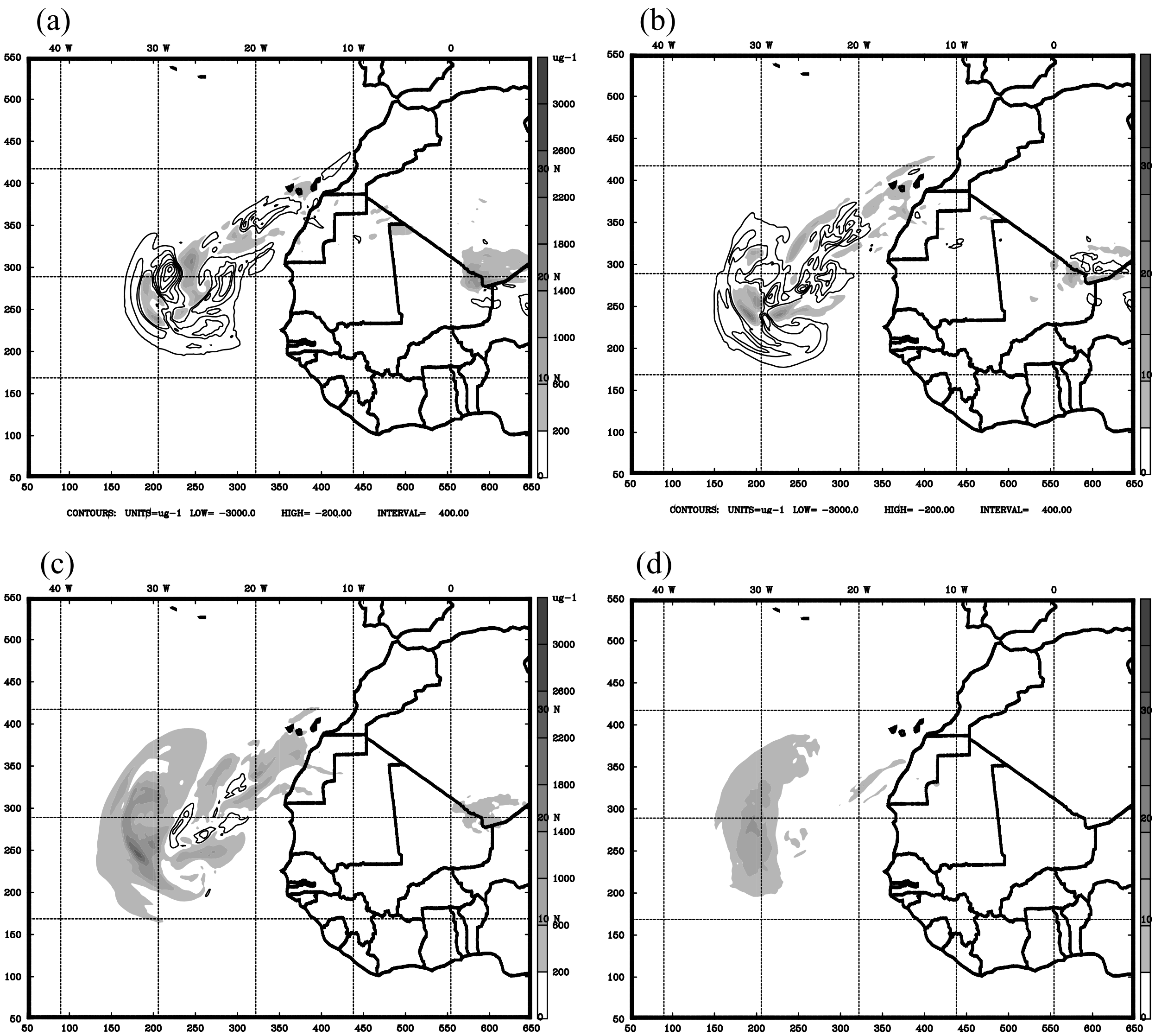

Figure 15. The difference of total dust mixing ratio (μg kg^{-1}) between ON and OFF (ON–OFF) at (a) 800 hPa, (b) 700 hPa, (c) 600 hPa, and (d) 500 hPa at 1200 UTC 20 July 2005 (60 h simulation). Shading (contour lines) indicate positive (negative) values. The contour line interval is 400 μg kg^{-1}.

the middle troposphere. After the inclusion of dust-radiation interactions, dust was able to penetrate higher than 500 hPa, reaching 8–9 km in height (Figures 15d and 6f). Therefore, simulated dust was more concentrated within a small region below the middle troposphere in ON than in OFF (Figures 15a and 15b; also see Figure 13a versus Figure 13b) and detrained above the middle troposphere (i.e., spread wider; Figures 15c and 15d). The difference in the vertically integrated total dust between ON and OFF (ON–OFF) shows that more dust was transported to the front end and north end of the plume, and less was left behind or south in ON. This is because in ON more dust was transported to the middle troposphere (~500 hPa), where winds were stronger to help transport dust downstream. Therefore, both the vertical and horizontal distributions of dust were modified by the dust-radiation interaction (Figures 15 and 16). As a result, the modification of dust distribution because of vertical motion and the change of static stability and wind profiles (i.e., horizontal winds) as well as the modification of moisture in response to the dust-radiation interaction can feedback to the heating profile. This will have a secondary effect on the shear alteration.

[29] The vertical shear and strength can have a strong impact on tropical cyclone activities. Therefore, the adjustment of the vertical shear because of the dust-radiation interactions and feedbacks can have an influence on hurricane activities, particularly over the region to the south of SAL where easterly wave disturbances and storms occur. To take a closer look at the vertical shear change, Figure 17a shows 60 h simulated vertical cross sections of the meridional temperature gradient and the vertical zonal wind shear at the south of SAL (along the thick line MN in Figure 5c) from OFF. The meridional temperature gradient within SAL was positive (i.e., warmer to the north and colder to the south)

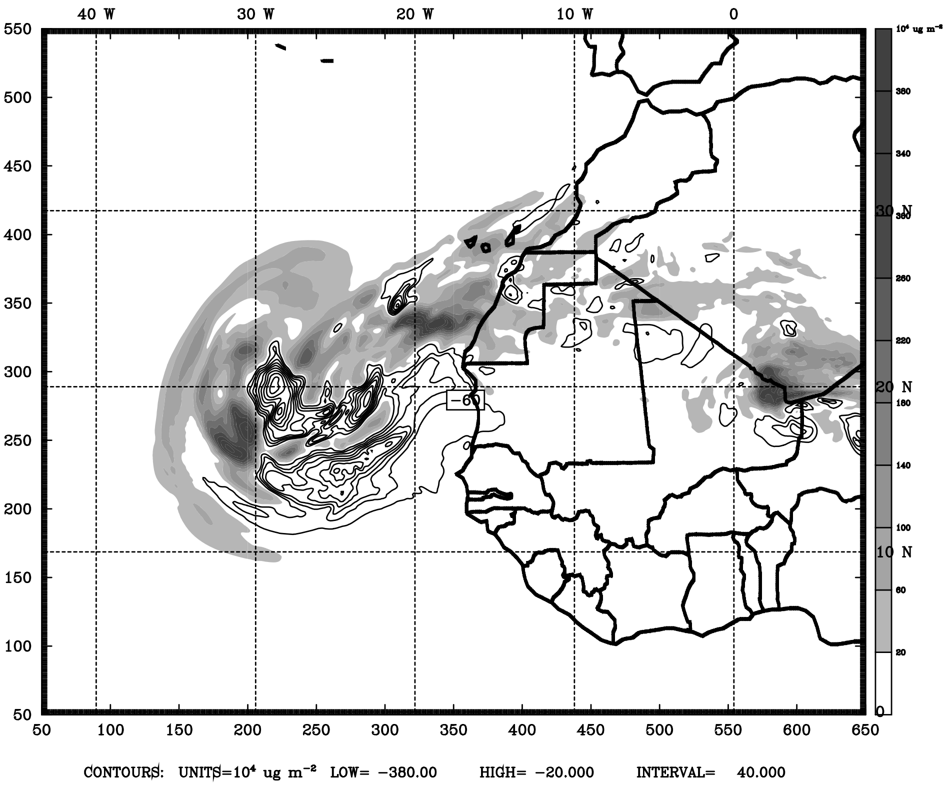

Figure 16. Difference of column integrated total dust ($\times 10^4$ μg m^{-2}) between ON and OFF (ON–OFF) at 1200 UTC 20 July 2005 (60 h simulation). Shading (contour lines) indicate positive (negative) values. The contour line interval is 40×10^4 μg m^{-2}.

and changed to a small negative value above the SAL. The vertical zonal wind shear matched the meridional temperature gradient very well from both experiments because of the thermal wind balance. Within the boundary layer, wind was mixed well vertically (Figure 18a). In the free atmosphere, the maximum vertical zonal wind shear became only slightly stronger (−6.0 m s^{-1} km^{-1} from OFF versus −6.2 m s^{-1} km^{-1} from ON) and the negative shear zone extended only slightly higher from ON after a 60 h integration. However, the strong shear zone (e.g., >5 m s^{-1} km^{-1}) expanded upward, and thus the shear became stronger between 750 hPa to 550 hPa (blue colors in the middle of Figure 17b), increasing by 1 to 2.0 m s^{-1} km^{-1}. The influence of the dust-radiation effect can also be seen from the vertical change of the zonal wind in which the maximum easterly wind was adjusted from 11.3 m s^{-1} from OFF to 14.4 m s^{-1} from ON over the dusty region after a 60 h integration. The maximum of the wind differences between ON and OFF reached 3.87 m s^{-1} (Figure 18b). Similar results were obtained at later times with slightly larger magnitudes (Figures 17c, 17d, 18c, and 18d). An enhanced vertical shear in the lower free atmosphere to the middle troposphere (750~500 hPa) can potentially inhibit hurricane genesis in this area (i.e., destroy the storm structure before it becomes a hurricane or tropical depression) and also potentially hinder hurricane intensification. Therefore, besides the cold sea surface temperature anomaly resulting from the dust extinction effect as shown in previous studies [*Evan et al.*, 2008], the modification of the vertical shear because of dust-radiation processes could be an additional cause of the inverse correlation between hurricane days and dust coverage proposed by *Evan et al.* [2006].

5. Concluding Remarks

[30] A tracer model based on the Weather Research and Forecasting (WRF) model was developed to study the effects of dust-radiation on the modification of the SAL and its environment, which can influence tropical cyclone (TC) activities over the Atlantic Ocean. Dust processes due to advection, boundary layer mixing, cumulus mixing, dry sedimentation, and dust-radiation interactions were included. However, the processes of moist deposition and dust-microphysics interactions were ignored in this study. Two numerical experiments, with (i.e., ON) and without (i.e., OFF) dust-radiation interactions, for a dust outbreak event were conducted. The model was integrated for 96 h.

[31] During 18–20 July 2005, a dust outbreak was clearly detected from satellite observations and was chosen for the examination of dust-radiation effects. The warm and dry SAL was well depicted by satellite retrievals. The dust plume was located toward the southern half of SAL. The aerosol optical depth (AOD) due to dust extinction at the wavelength of 0.55 μm was as high as 1.5 and reached a maximum of 4, which was potentially overestimated because of the existence of low-level clouds. The temperature difference between

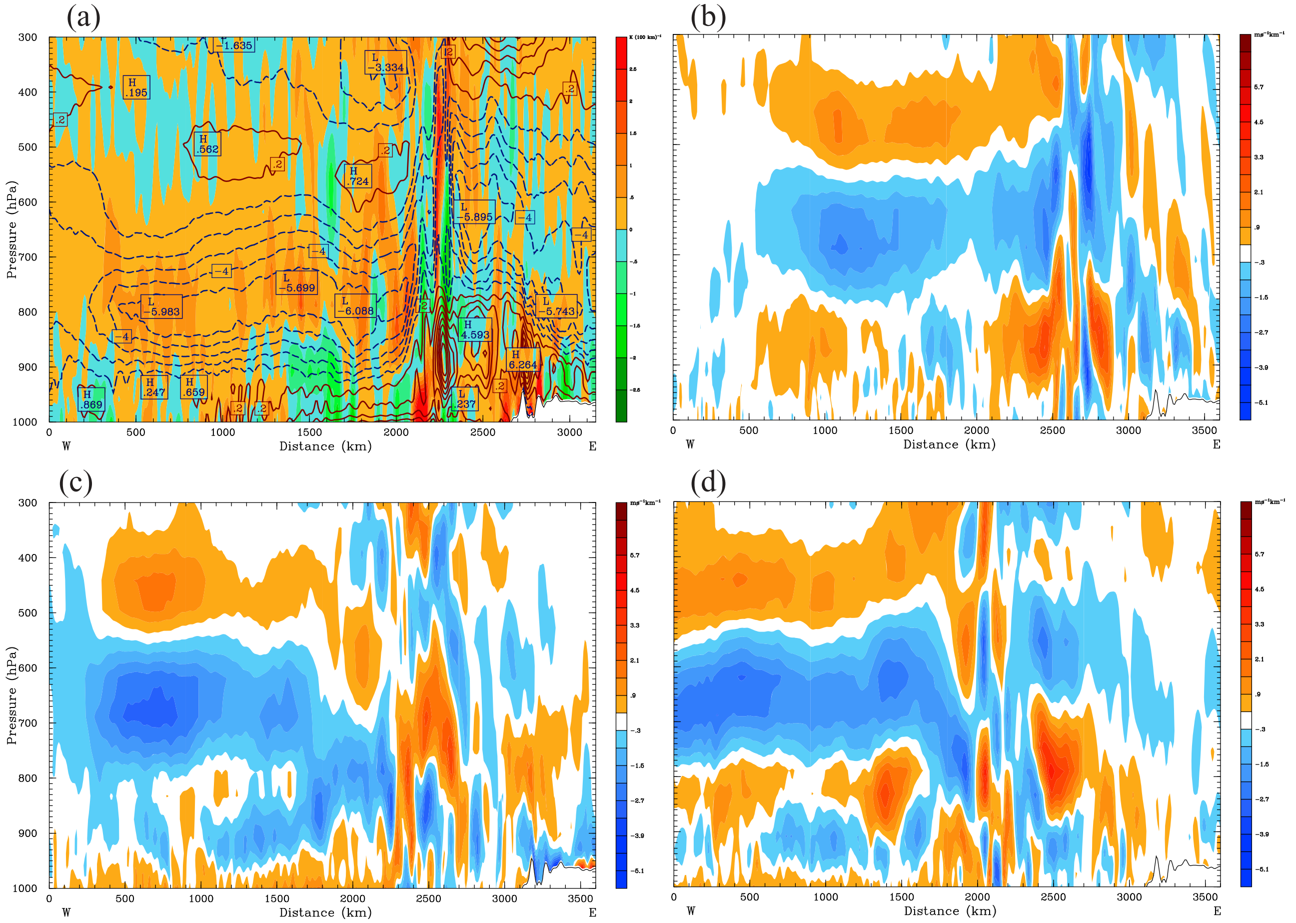

Figure 17. (a) The vertical cross sections (thick black line MN in Figure 5c) of vertical east-westerly wind shear (m s^{-1}, contour lines) and meridional temperature gradient ($\partial T/\partial y$; K/100 km) from OFF at 1200 UTC 20 July 2005 after a 60 h integration. (b, c, and d) Difference of the vertical wind shear between ON and OFF (ON–OFF) after 60 h, 72 h, and 84 h simulations, respectively.

a dusty column and a relatively clean column reached 3 K in the warm anomaly around 700 hPa and −6 K in the cold anomaly near the surface from satellite retrievals.

[32] The inclusion of the dust-radiation effects (i.e., ON) improved the location of the 700 hPa maximum temperature such that it compared better with satellite retrievals. However, the simulated maximum temperature at 700 hPa from ON was higher than satellite data (~2 K). The primary reason might be the overestimation of dust shortwave absorption [*Colarco et al.*, 2002; *Sinyuk et al.*, 2003]. The dust-radiation interactions enhanced the vertical transport of dust, which reached up to an 8–9 km height, similar to what was discussed by *Liu et al.* [2003]. The simulated clear-sky downward shortwave radiation at the surface around noon was reduced by dust scattering and absorption by more than 400 W m^{-2} and cooled the surface maximum temperature by about 9 K.

[33] At the dust plume region over ocean, the air was maximally heated at 600 to 700 hPa levels because of the dust shortwave absorption that dominated the dust longwave cooling. Another local heating maximum was found in the lower boundary layer because of the dominance of downward longwave heating from dust emission aloft. In addition to the direct effect on the radiation budget, dust-radiation interactions could induce positive moisture anomalies at most of the dusty region and modify the dust distribution through the change of the winds and static stability, both secondary effects (feedbacks) on the radiation budget. These feedbacks further altered temperature profiles. Further study is required to understand the mechanism linking the dust-radiation effect and increased moisture.

[34] The modification of the north-south temperature gradient because of the dust-radiation direct and indirect effects altered zonal wind profiles and vertical wind shear. To the south of the maximum dust concentration where the easterly wave and tropical storms develop, simulated dust-radiation effects reduced the easterly wind component between the lower troposphere and about 650 hPa, and increased the easterly wind component between about 650 hPa and 500 hPa. Further analysis showed that the strength of the vertical shear intensified by about 1 to 2.5 m s^{-1} km^{-1} between approximately 750 hPa and 550 hPa (i.e., the maximum vertical wind shear layer expanded), resulting in a maximum wind change of 3~5 m s^{-1}, a 30~40% increase, around the top of this layer. The dust-radiation effect might

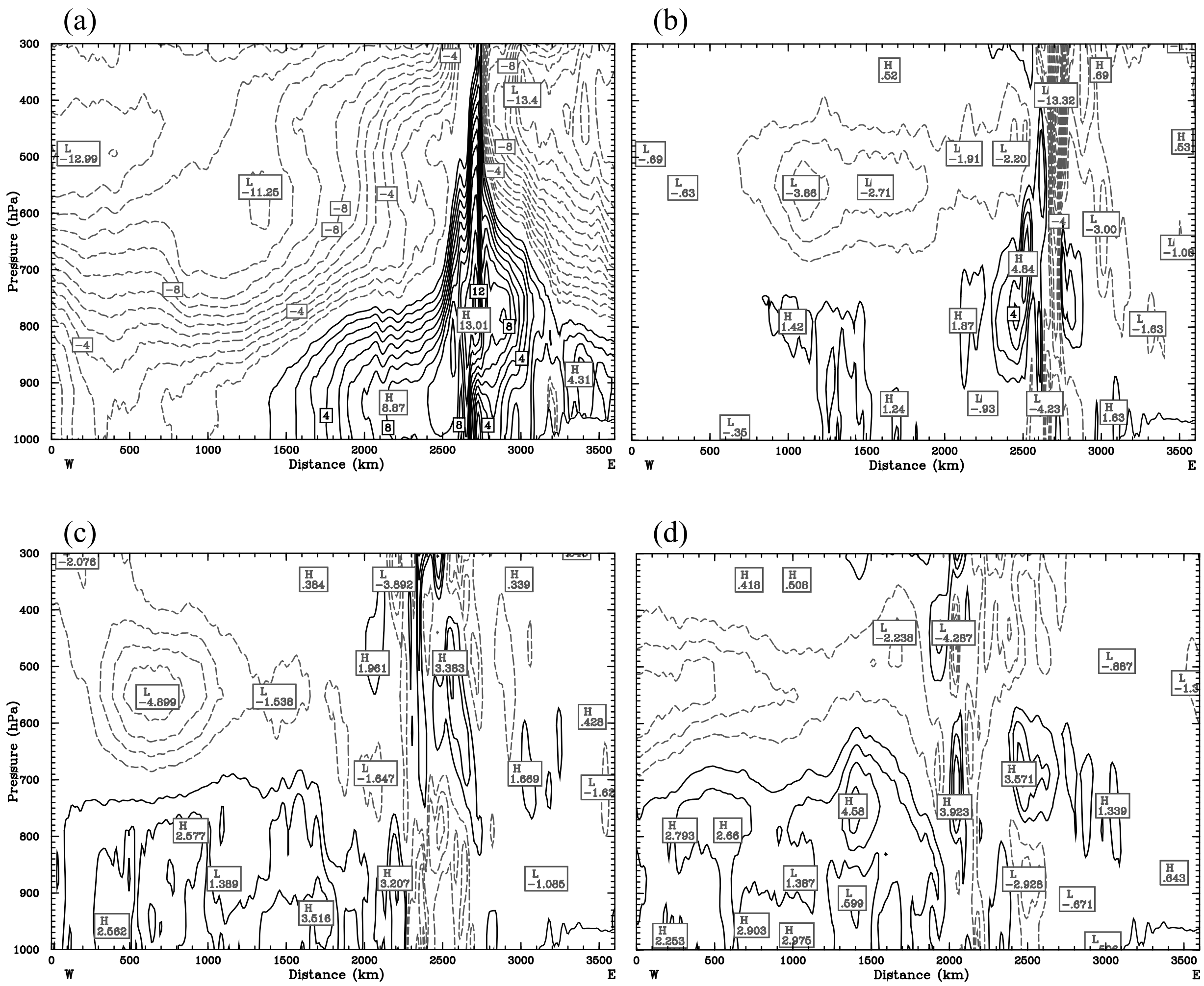

Figure 18. (a) The vertical cross sections (thick black line MN in Figure 5c) of the east-westerly wind (m s^{-1}, positive solid lines and negative dashed lines) from OFF at 1200 UTC 20 July 2005 after a 60 h integration. (b, c, and d) Difference of the east-westerly wind between ON and OFF (ON–OFF) after 60 h, 72 h, and 84 h simulations, respectively.

have an impact, but is one of many, on tropical cyclone genesis. Links between dust-radiation interactions and actual tropical cyclone genesis still remain to be explored.

[35] This study explored the dust-radiation effects on the modification of SAL and its environmental shear. The modification of vertical wind shear studied here is probably at the high end of the spectrum because of the use of a strong dust outbreak event. A wider range of case studies is required in order to give a more general conclusion, and these will be conducted in the future. Moreover, the influence of the environmental modification by dust-radiation processes on tropical cyclone genesis and intensification will be investigated as well.

[36] **Acknowledgments.** The authors would like to acknowledge the WRF teams for their efforts on model development. We would also like to thank Scott Braun, Jiun-Dar Chern, Lorraine Remer, Richard Kleidman, and Mian Chin at NASA/GSFC, Ming-Da Chou at National Taiwan University, and Kuo-Nan Liou at University of California, Los Angeles, for their scientific discussions. Thanks are further extended to the editor Steven Ghan and three anonymous reviewers for their valuable scientific comments on the manuscript. The MODIS and AIRS data and images were requested from the MODIS-atmosphere web site from NASA/GSFC and the NASA Goddard Earth Sciences Data and Information Services Center. One of the coauthors, S.-H. Wang, acknowledges support from Taiwan's National Science Council (NSC92-2111-M-008-018-AGC), Taiwan EPA (EPA94-U1L1-02-101), and the NASA Radiation Science Program (managed by Hal Maring). This work is primarily supported by the NASA Hurricane Science Research Program (grant NNX09AC38G) that is directed by Ramesh Kakar at NASA Headquarters.

References

Braun, S. (2010), Reevaluating the role of the Saharan air layer in Atlantic tropical cyclogenesis and evolution, *Mon. Weather Rev.*, *138*, 2007–2037, doi:10.1175/2009MWR3135.1.

Carlson, T. N., and S. G. Benjamin (1980), Radiative heating rates for Saharan dust, *J. Atmos. Sci.*, *37*, 193–213, doi:10.1175/1520-0469(1980)037<0193:RHRFSD>2.0.CO;2.

Chen, G., et al. (2010), Observations of Saharan dust microphysical and optical properties from the eastern Atlantic during NAMMA airborne field campaign, *Atmos. Chem. Phys. Discuss.*, *10*, 13,445–13,493, doi:10.5194/acpd-10-13445-2010.

Chen, S.-H., and W.-Y. Sun (2002), A one-dimensional time-dependent cloud model, *J. Meteorol. Soc. Jpn.*, *80*, 99–118, doi:10.2151/jmsj.80.99.

Chen, S.-H., J. Dudhia, J. S. Kain, T. Kindap, and E. Tan (2008), Development of the on-line MM5 tracer model and its applications to air pollution episodes in Istanbul, Turkey and Sahara dust transport, *J. Geophys. Res.*, *113*, D11203, doi:10.1029/2007JD009244.

Chin, M., T. Diehl, O. Dubovik, T. F. Eck, B. N. Holben, A. Sinyuk, and D. G. Streets (2009), Light absorption by pollution, dust, and biomass burning aerosols: A global model study and evaluation with AERONET measurements, *Ann. Geophys.*, *27*, 3439–3464, doi:10.5194/angeo-27-3439-2009.

Chou, M.-D., and M. J. Suarez (1999), A solar radiation parameterization for atmospheric studies, *NASA Tech. Memo., TM-104606*, vol. no. 15, 40 pp.

Chou, M.-D., M. J. Suarez, X.-Z. Liang, and M. M.-H. Yan (2001), A thermal infrared radiation parameterization for Atmospheric Studies, *NASA Tech. Memo., TM-104606*, vol. no. 19, 102 pp.

Colarco, P. R., O. B. Toon, O. Torres, and P. J. Rasch (2002), Determining the UV imaginary index of refraction of Saharan dust particles from Total Ozone Mapping Spectrometer data using a three-dimensional of dust transport, *J. Geophys. Res.*, *107*(D16), 4289, doi:10.1029/2001JD000903.

Dunion, J. P., and C. S. Velden (2004), The impact of the Saharan air layer on Atlantic tropical cyclone activity, *Bull. Am. Meteorol. Soc.*, *85*, 353–365, doi:10.1175/BAMS-85-3-353.

Evan, A. T., J. Dunion, J. A. Foley, A. K. Heidinger, and C. S. Velden (2006), New evidence for a relationship between Atlantic tropical cyclone activity and African dust outbreaks, *Geophys. Res. Lett.*, *33*, L19813, doi:10.1029/2006GL026408.

Evan, A. T., A. K. Heidinger, R. Bennartz, V. Bennington, N. M. Mahowald, H. Corrada-Bravo, C. S. Velden, G. Myhre, and J. P. Kossin (2008), Ocean temperature forcing by aerosols across the Atlantic tropical cyclone development region, *Geochem. Geophys. Geosyst.*, *9*, Q05V04, doi:10.1029/2007GC001774.

Foltz, G. R., and M. J. McPhaden (2008), Impact of Saharan dust on tropical North Atlantic SST, *J. Clim.*, *21*, 5048–5060, doi:10.1175/2008JCLI2232.1.

Gillette, D. (1978), A wind tunnel simulation of the erosion of soil: Effect of soil texture, sandblasting, wind speed, and soil consolidation on dust production, *Atmos. Environ.*, *12*, 1735–1743, doi:10.1016/0004-6981(78)90322-0.

Gray, W. M. (1968), Global view of the origin of tropical disturbances and storms, *Mon. Weather Rev.*, *96*, 669–700, doi:10.1175/1520-0493(1968)096<0669:GVOTOO>2.0.CO;2.

Haywood, J., et al. (2008), Overview of the dust and biomass burning experiment and African monsoon multidisciplinary analysis special observing period-0, *J. Geophys. Res.*, *113*, D00C17, doi:10.1029/2008JD010077.

Hess, M., P. Kopke, and I. Schult (1998), Optical properties of aerosols and clouds: The software package OPAC, *Bull. Am. Meteorol. Soc.*, *79*, 831–844, doi:10.1175/1520-0477(1998)079<0831:OPOAAC>2.0.CO;2.

Hong, S.-Y., and H.-L. Pan (1996), Nonlocal boundary layer vertical diffusion in a medium-range forecast model, *Mon. Weather Rev.*, *124*, 2322–2339, doi:10.1175/1520-0493(1996)124<2322:NBLVDI>2.0.CO;2.

Hsu, N. C., S. Tsay, M. D. King, and J. R. Herman (2004), Aerosol properties over bright-reflecting source regions, *IEEE Trans. Geosci. Remote Sens.*, *42*, 557–569, doi:10.1109/TGRS.2004.824067.

Johnson, B. T., B. Heese, S. A. McFarlane, P. Chazette, A. Jones, and N. Bellouin (2008), Vertical distribution and radiative effects of mineral dust and biomass burning aerosol over West Africa during DABEX, *J. Geophys. Res.*, *113*, D00C12, doi:10.1029/2008JD009848.

Jones, C., N. Mahowald, and C. Luo (2004), Observational evidence of African desert dust intensification of easterly waves, *Geophys. Res. Lett.*, *31*, L17208, doi:10.1029/2004GL020107.

Jones, T. A., D. J. Cecil, and J. Dunion (2007), The environmental and inner-core conditions governing the intensity of Hurricane Erin (2001), *Weather Forecast.*, *22*, 708–725, doi:10.1175/WAF1017.1.

Kain, J. S. (2004), The Kain-Fritsch convective parameterization: An update, *J. Appl. Meteorol.*, *43*, 170–181, doi:10.1175/1520-0450(2004)043<0170:TKCPAU>2.0.CO;2.

Karyampudi, V. M., and T. N. Carlson (1988), Analysis and numerical simulations of the Saharan air layer and its effect on easterly wave disturbances, *J. Atmos. Sci.*, *45*, 3102–3136, doi:10.1175/1520-0469(1988)045<3102:AANSOT>2.0.CO;2.

Karyampudi, V. M., and H. F. Pierce (2002), Synoptic-scale influence of the Saharan air layer on tropical cyclogenesis over the eastern Atlantic, *Mon. Weather Rev.*, *130*, 3100–3128, doi:10.1175/1520-0493(2002)130<3100:SSIOTS>2.0.CO;2.

Karyampudi, V. M., et al. (1999), Validation of the Saharan dust plume conceptual model using lidar, Meteosat, and ECMWF data, *Bull. Am. Meteorol. Soc.*, *80*, 1045–1075, doi:10.1175/1520-0477(1999)080<1045:VOTSDP>2.0.CO;2.

Kaufman, Y. J., et al. (2005), A critical examination of the residual cloud contamination and diurnal sampling effects on MODIS estimates of aerosol over ocean, *IEEE Trans. Geosci. Remote Sens.*, *43*, 2886–2897, doi:10.1109/TGRS.2005.858430.

Krishnamurti, T. N., S. Pattnaik, L. Stefanova, T. S. V. Vijaya Kumar, B. P. Mackey, and A. J. O'Shay (2005), The hurricane intensity issue, *Mon. Weather Rev.*, *133*, 1886–1912, doi:10.1175/MWR2954.1.

Landsea, C. W. (1993), A climatology of intense (or major) Atlantic hurricanes, *Mon. Weather Rev.*, *121*, 1703–1713, doi:10.1175/1520-0493(1993)121<1703:ACOIMA>2.0.CO;2.

Lau, K. M., and J. M. Kim (2007), Cooling of the Atlantic by Saharan dust, *Geophys. Res. Lett.*, *34*, L23811, doi:10.1029/2007GL031538.

Léon, J.-F., Y. Derimian, I. Chiapello, D. Tanré, T. Podvin, B. Chatenet, A. Diallo, and C. Deroo (2009), Aerosol vertical distribution and optical properties over M'Bour (16.96° W; 14.39° N), Senegal from 2006 to 2008, *Atmos. Chem. Phys.*, *9*, 9249–9261, doi:10.5194/acp-9-9249-2009.

Li, F., A. M. Vogelmann, and V. Ramanathan (2004), Saharan dust aerosol radiative forcing measured from space, *J. Clim.*, *17*, 2558–2571, doi:10.1175/1520-0442(2004)017<2558:SDARFM>2.0.CO;2.

Liu, M., D. L. Westphal, S. Wang, A. Shimizu, N. Sugimoto, J. Zhou, and Y. Chen (2003), A high-resolution numerical study of the Asian dust storms of April 2001, *J. Geophys. Res.*, *108*(D23), 8653, doi:10.1029/2002JD003178.

Mainelli, M., M. DeMaria, L. K. Shay, and G. Goni (2008), Application of oceanic heat content estimation to operational forecasting of Atlantic category 5 hurricanes, *Weather Forecast.*, *23*, 3–16, doi:10.1175/2007WAF2006111.1.

Pratt, A. S., and J. L. Evans (2009), Potential impacts of the Saharan air layer on numerical model forecasts of North Atlantic tropical cyclogenesis, *Weather Forecast.*, *24*, 420–435, doi:10.1175/2008WAF2007090.1.

Reale, O., W. K. Lau, K.-M. Kim, and E. Brin (2009), Atlantic tropical cyclogenetic processes during SOP-3 NAMMA in the GEOS-5 global data assimilation and forecast system, *J. Atmos. Sci.*, *66*, 3563–3578, doi:10.1175/2009JAS3123.1.

Redemann, J., Q. Zhang, P. B. Russell, J. M. Livingston, and L. A. Remer (2009), Case studies of aerosol remote sensing in the vicinity of clouds, *J. Geophys. Res.*, *114*, D06209, doi:10.1029/2008JD010774.

Remer, L. A., et al. (2005), The MODIS aerosol algorithm, products, and validation, *J. Atmos. Sci.*, *62*, 947–973, doi:10.1175/JAS3385.1.

Rogers, R., et al. (2006), The intensity forecasting experiment: A NOAA multiyear field program for improving tropical cyclone intensity forecasts, *Bull. Am. Meteorol. Soc.*, *87*, 1523–1537, doi:10.1175/BAMS-87-11-1523.

Shu, S., and L. Wu (2009), Analysis of the influence of the Saharan air layer on tropical cyclone intensity using AIRS/Aqua data, *Geophys. Res. Lett.*, *36*, L09809, doi:10.1029/2009GL037634.

Sinyuk, A., O. Torres, and O. Dubovik (2003), Combined use of satellite and surface observations to infer the imaginary part of refractive index of Saharan dust, *Geophys. Res. Lett.*, *30*(2), 1081, doi:10.1029/2002GL016189.

Skamarock, W. C., J. B. Klemp, J. Dudhia, D. O. Gill, D. M. Barker, M. G. Duda, X.-Y. Huang, W. Wang, and J. G. Powers (2008), A Description of the advanced research WRF version 3, *Tech. Note, NCAR/TN-475+STR*, XXXXX.

Soil Survey Division Staff (1993), *Soil Survey Manual*, U.S. Dep. of Agric., Washington, D. C.

Sun, D., K. M. Lau, and M. Kafatos (2008), Contrasting the 2007 and 2005 hurricane seasons: Evidence of possible impacts of Saharan dry air and dust on tropical cyclone activity in the Atlantic basin, *Geophys. Res. Lett.*, *35*, L15405, doi:10.1029/2008GL034529.

Sun, D., W. K. M. Lau, M. Kafatos, Z. Boybeyi, G. Leptoukh, and C. Yang (2009), Numerical simulations of the impacts of the Saharan air layer on Atlantic tropical cyclone development, *J. Clim.*, *22*, 6230–6250, doi:10.1175/2009JCLI2738.1.

Tegen, I., and I. Fung (1994), Modeling of mineral dust in the atmosphere: Sources, transport, and optical thickness, *J. Geophys. Res.*, *99*, 22,897–22,914, doi:10.1029/94JD01928.

Tegen, I., and A. A. Lacis (1996), Modeling of particle size distribution and its influence on the radiative properties of mineral dust aerosol, *J. Geophys. Res.*, *101*, 19,237–19,244, doi:10.1029/95JD03610.

Wang, C., G.-R. Jeong, and N. Mahowald (2009), Particulate absorption of solar radiation: Anthropogenic aerosols vs. dust, *Atmos. Chem. Phys. Discuss.*, *9*, 6571–6595, doi:10.5194/acpd-9-6571-2009.

Wang, S.-H., N.-H. Lin, M.-D. Chou, and J.-H. Woo (2007), Estimate of radiative forcing of Asian biomass-burning aerosols during the period of TRACE-P, *J. Geophys. Res.*, *112*, D10222, doi:10.1029/2006JD007564.

Wong, S., and A. E. Dessler (2005), Suppression of deep convection over the tropical North Atlantic by the Saharan air layer, *Geophys. Res. Lett.*, *32*, L09808, doi:10.1029/2004GL022295.

Wong, S., A. E. Dessler, N. M. Mahowald, P. R. Colarco, and A. da Silva (2008), Long-term variability in Saharan dust transport and its link to North Atlantic sea surface temperature, *Geophys. Res. Lett.*, *35*, L07812, doi:10.1029/2007GL032297.

Wong, S., A. E. Dessler, N. M. Mahowald, P. Ying, and Q. Feng (2009), Maintenance of lower tropospheric temperature inversion in the Saharan air layer by dust and dry anomaly, *J. Clim.*, *22*, 5149–5162, doi:10.1175/2009JCLI2847.1.
Wu, L. (2007), Impact of Saharan air layer on hurricane peak intensity, *Geophys. Res. Lett.*, *34*, L09802, doi:10.1029/2007GL029564.
Zhang, J., J. S. Reid, and B. N. Holben (2005), An analysis of potential cloud artifacts in MODIS over ocean aerosol optical thickness products, *Geophys. Res. Lett.*, *32*, L15803, doi:10.1029/2005GL023254.
Zhu, A., V. Ramanathan, F. Li, and D. Kim (2007), Dust plumes over the Pacific, Indian, and Atlantic oceans: Climatology and radiative impact, *J. Geophys. Res.*, *112*, D16208, doi:10.1029/2007JD008427.
Zipser, E. J., et al. (2009), The Saharan air layer and the fate of African easterly waves—NASA's AMMA Field Study of Tropical Cyclogenesis, *Bull. Am. Meteorol. Soc.*, *90*, 1137–1156, doi:10.1175/2009BAMS2728.1.

S.-H. Chen and M. Waylonis, Department of Land, Air, and Water Resources, University of California, Davis, One Shields Avenue, Davis, CA 95616, USA. (shachen@ucdavis.edu)

S.-H. Wang, Department of Atmospheric Sciences, National Central University, Chung-Li, Taiwan.